INTERPLAY BETWEEN MAGNETISM AND SUPERCONDUCTIVITY IN THE CUPRATES

AMIT KANIGEL

INTERPLAY BETWEEN MAGNETISM AND SUPERCONDUCTIVITY IN THE CUPRATES

RESEARCH THESIS

SUBMITTED IN PARTIAL FULFILLMENT OF THE

REQUIREMENTS

FOR THE DEGREE OF DOCTOR OF SCIENCE

AMIT KANIGEL

ACKNOWLEDGMENT

Contents

List of Figures

List of Tables

Abstract

In the present work we describe an effort made to find correlation between super-conductivity and magnetism in the cuprates. Most of the work was done using the CLBLCO system, which is less known than the canonical cuprates, but offers nice flexibility of the phase diagram. Using zero field (ZF) and transverse field (TF) μSR we characterized many samples and constructed the phase diagram of the system, including the superconductivity transition temperature (T_c) and the spin-glass transition temperature (T_g). Using a scaling relation we showed that T_c and T_g are correlated in way that leave no doubt about the importance of the magnetic correlation in the superconductivity mechanism of the cuprates. We also extended the scaling relation to other, more commonly studied, systems and found that the T_c-T_g relation is universal.

Chapter 1

PREFACE

The new high Tc superconductors that were discovered in the mid 80's are based on doped materials that in their undoped state are antiferromagnetic (AF). Actually, before these materials were found to be superconductors they were considered to be the best example of two-dimensional quantum Heisenberg magnets. It is believed, that the origin of the superconductivity in the cuprates lies in the copper-oxide (CuO_2) planes, which are also the origin of the magnetism at low doping levels.

Upon doping, the Neel temperature decreases up to some doping level, at which an ordered antiferromagnetic state can not be found any more. This doping level is very small, usually a few percents of holes in the CuO_2 planes are enough. Above some doping level, superconductivity (SC) emerges, this is shown schematically in figure 1.1.

The superconducting phase in all the cuprates has common features. They are all type II SC. The coherence length was found to be very short, of the same order as the unit cell. The superconductivity in these materials is very anisotropic, and the penetration depth of a field applied parallel to the CuO_2 planes can be up to 50 times
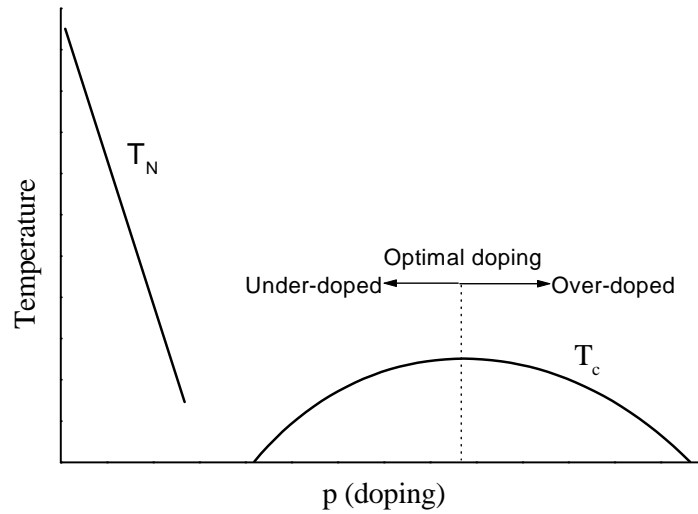
Figure 1.1: The main features of the phase diagram of the cuprates.
המאפיינים העיקריים של דיאגרמת הפאזות של הקופרטיס.

larger then the penetration depth of a field applied normal to the planes.

The critical temperature increases with the doping up to some point known as the "optimal doping" point, increasing the doping further results in a reduction in Tc. The doping regimes below and above the optimal doping are known as the underdoped and overdoped regimes, respectively.

Many works have shown that the boundary between AF and SC is not at all sharp, meaning that AF correlations still exist in these compounds even at high doping levels and in the SC state. Theoretically is hard to accept that magnetism and SC can coexist, when it is known that the BCS state is completely destroyed by a small amount of magnetic impurities. And, in fact, for many years those samples that showed both magnetism and SC were considered to be bad samples.

On the other hand, the small coherence length, and the fact that there are AF

correlations in the CuO_2 planes, led many researchers to suggest that the origin of the superconductivity in the cuprates is magnetic.

The goal of this work is to provide an experimental proof to the very important role that magnetism and the AF correlations play in the superconductivity mechanism. For that we focus on the regime in the phase diagram in which superconductivity and magnetism coexist. We choose as the case test the CLBLCO system that has some properties that makes it suitable for our purpose. We did careful μSR measurement on many samples. Using TF (transverse field) μSR we measured the in-plane penetration depth and using ZF (zero field) μSR we measured the freezing temperature of the moments and the spin configuration at base temperature. We observed several results:

1. The CLBLCO system satisfies the relation between the penetration depth and T_c known as the Uemura plot.

2. At base temperature the samples phase separate, on a microscopic length scale.

3. T_g, the temperature at which the moments freeze into a disordered magnet, is highly correlated with the superconductivity transition temperature.

In the rest of this chapter we review experimental evidence for AF correlation in the SC state, focusing on NMR/NQR and μSR data. In chapter 2 we review a theoretical model which predicts correlations between magnetism and superconductivity in the cuprates. Then in chapter 3, we introduce the CLBLCO system with its special properties. In chapter 4, we explain the experimental aspects of the work, including μSR and magnetization measurements. Finally, in chapter 5, the results are shown and discussed.

1.1 Evidence for Antiferromagnetic correlations in the cuprates.

Evidence for AF correlation in the cuprates, even in the SC state, was found soon after the discovery of the HTSC. The magnetism can be seen in a variety of experimental techniques, NMR, μSR, neutron scattering and more. We focus on NMR and μSR.

1.1.1 NMR

We describe two experiments. The first, done on pure samples of YBCO reveals differences between the temperature dependence of the relaxation times of different nuclei in the same sample. The second one was done on impurity doped samples.

Using NMR the local spin susceptibility can be measured as the shift of the NMR signal. The shift of both O and Cu in YBCO have the same temperature dependence and can be explained using the single spin fluid model [1]. Takigawa *et. al.* [2] were the first to notice the different temperature dependences of relaxation times, T_1, of the O and Cu sites.

In the single spin fluid picture it is assumed that the only spin in the problem is the Cu^{2+} ($S = 1/2$) spin. Then, the resonance shift of the difference nuclei will be $K^{Nu} = A^{Nu}\xi(q = 0)H_{ext}$ where A^{NU} are the different hyperfine coupling constants of the different nuclei. On the other hand the relaxation times T_1 are related to the imaginary part of the spin susceptibility in the form: $\frac{1}{T_1 T} \propto \sum_q A_q^2 \frac{\xi''(q,\omega)}{\omega}$ where A_q are the form factors which are related to the position of the nuclei in the lattice, and ω is the resonance frequency. The origin of the difference between the O and Cu relaxation times is in the different form factors. While the form factor of the O is peaked around $q = 0$ the form factor of the Cu is peaked around $q = q_{AF}$.

This indicates that the behavior of the spin susceptibility at $q = 0$ and $q = q_{AF}$ is very different, and in turn it points to the presence of antiferromagnetic spin activity very deep in the superconducting phase.

The measurement of the static part of the AF spin susceptibility in the plane is possible using NMR. By substituting 1% of the Cu by nonmagnetic impurities like Ni or Zn one can measure in an indirect way $\xi(q = q_{AF})$.

Although Zn is not magnetic, it induces magnetic sites in the planes which have Curie like behavior [3]. By Measuring the line shape of the planar Cu, Julien *et. al.* deduced that the Zn induces a staggered field in its vicinity. This magnetic field decays rather fast, on a length scale of a few lattice constants. They could not tell what is the exact real space shape of the susceptibility in their experiment.

Bobrrof *et. al.* reach very similar conclusions using Li NMR. ¿From these experiments it is deduced that the nonmagnetic impurities just enhance the already existing AF correlations, and slow down their fluctuation rate to make them observable using NMR. This again points to the fact that enhanced AF correlations still exist in the CuO_2 planes even in the superconducting phase.

1.1.2 μSR

Muons are the most sensitive probe for local magnetic fields, the principles of the μSR technique will be explained in chapter 4. In this section we would like to describe the findings of two groups using μSR in cuprates. Niedermayer *et. al.* [4] performed μSR measurements on two families of HTSC, $La_{2-x}Sr_xCuO_4$ and $Y_{1-x}Ca_xBa_2Cu_3O_6$, in the low doping regime. They found that the Neel state disappears at a hole density of around $p_{sh} \sim 0.02$ and is replaced by a disordered state of frozen moments, which have much in common with a spin-glass. They constructed a common phase diagram

for both compounds and found similar behavior. The spin-glass phase penetrates into the SC regime.

Panagopoulos *et. al.* [5] performed a similar experiment on different systems including Zn doped systems. They, again, found the spin glass phase in all the systems they checked.

There were many earlier works that found disordered magnetism in the cuprates away from the AF regime. The importance of these two works is especially in that they measure many samples in a systematic way, and show that the spin glass phase is an intrinsic part of the phase diagram of the cuprates.

1.2 Plaquette Boson Fermion Model(PBFM) and the SO(5) model

Recently Altman and Auerbach [6] derived an effective Hamiltonian from the Hubbard model that describes correctly many of the cuprates properties. The Hubbard model is given by: $\mathcal{H} = -t \sum_{<ij>,s}(c_{is}^{\dagger}c_{js} + H.c) + U \sum_i n_{i\uparrow}n_{i\downarrow}$, where $c_{is}^{\dagger}$, n_{is} are electron creation and number operators at site i, t is the hopping integral and U is the on-site interaction.

The effective Hamiltonian is constructed by solving the Hubbard model on a square plaquette of 4 sites and keeping only the low energy states. One can identify with these states 4 different bosons : a hole pair and an antiferromagnetic magnon triplet, and fermionic states that involve one hole on the plaquette.

On one plaquette it was found that there is pair binding for some range of the Hubbard parameters U and t, coming from the minimization of the number of broken

bonds that achieved pairing. Furthermore, there is another kinetic pairing mecha-
nism, which extends the parameters range in which pairing is found.

The authors calculated the interplaquette interaction and obtained an effective
Hamiltonian

$$\mathcal{H}^{4b} = \mathcal{H}^b[b] + \mathcal{H}^t[t] + \mathcal{H}^{int}[b,t]$$

written in term of bosonic creation operators. $b^\dagger$, $t^\dagger$ are the creation operators of the
hole pair and of the magnons.

$$\mathcal{H}^b = (\epsilon_b - 2\mu) \sum_i b_i^\dagger b_i - J_b \sum_{<i,j>} (b_i^\dagger b_j + H.c)$$

is the hole pair part which contains a term that is proportional to number of pairs in
the lattice and an hopping term.

$$\mathcal{H}^t = \epsilon_t \sum_{i\alpha} t_{i\alpha}^\dagger t_{i\alpha}^\dagger - \frac{J_t}{2} \sum_{\alpha<ij>} (t_{\alpha i}^\dagger t_{\alpha j}^\dagger + H.c.)$$

is the triplet part and $\mathcal{H}^{int}$ is the part which describes the interaction between different
bosons. This Hamiltonian does not include fermionic contributions.

Figure 1.2 describes the hopping energy of the various bosons between the plaque-
ttes. The main result is the correlation between the hopping energies of the magnons
and the hole pair. At $U = 8t$ they are equal, and in all the range in which pairing
exists they are almost equal [6].

We believe that this issue is not trivial at all, and it is a prediction that can be
tested experimentally. To test this prediction we must find an experimental quantity
that is sensitive to J_b and J_t. For this purpose it is beneficial to look at the mean
field treatment of this model.

The uniform mean field approximation to this Hamiltonian [7] amounts to replac-
ing the bosonic operators by their average expectation values. Minimizing the $T = 0$
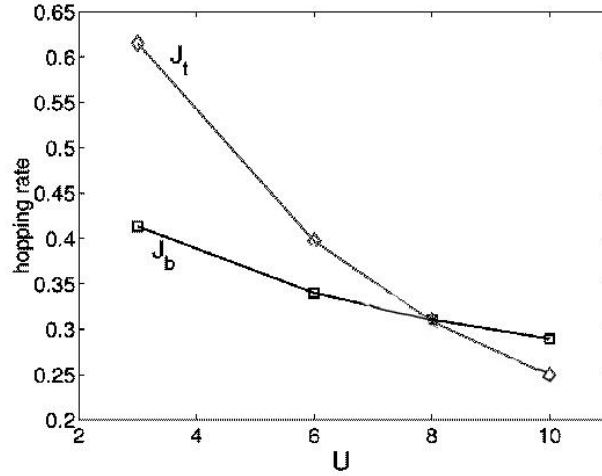
Figure 1.2: Boson hopping energies versus U/t. J_t is the magnon hopping energy. J_b is the pair hopping energy. Taken from [6]

אנרגיית הקפיצה של הבוזונים השונים.

variational energy it was found that there is a first order phase transition at a critical value of the chemical potential, μ_c. At $\mu < \mu_c$ the ground state consists of a Mott insulator with no hole pairs and with a finite staggered magnetization. For $\mu > \mu_c$ the ground state is a d-wave superconductor with an order parameter $|<b_h^\dagger>|^2$.

So we see that the model contains the main features of the cuprates, a Mott insulator that above some critical doping level becomes doped with hole pairs. These phase transition govern all the low temperature behavior of these systems. Due to the other terms present in the Hamiltonian, the fermionic terms and the Coulomb interaction term, this phase transition is less sharp in doping, and many intermediate phases exist. These phases represent solutions which are non uniform, cases in which the system phase separates into domains that can have quite complicated topological shapes. Furthermore, even the weakest disorder can be important in determining the exact way in which the phases separate.

This region in the phase diagram is the most interesting for our purpose because it enables us to find a single sample with measurable properties that are sensitive to both the parameters that govern the superconducting phase and to those that govern the magnetic phase.

1.2.1 Relation between T_c and J_b

The superconducting transition temperature can be shown to be related to J_b. To see that we analyze the kinetic energy term of the hole pairs, we replace b_i with $\sqrt{n}e^{-i\phi(i)}$ where n is the superfluid density and $\phi(i)$ is a local phase. Then expanding the exponent we obtained for the kinetic energy of the bosons:

$$\mathcal{H} \propto \sum_i J_b n (\nabla \phi)^2$$

. We obtained for the kinetic energy an Hamiltonian that looks like an XY model in 2D[8], where the stiffness of the model is given by:

$$\rho_b = J_b n$$

The X-Y model in 2D is known to have a Kosterlitz-Thouless phase transition. The low temperature phase has a quasi-ordered state which is characterized by an algebraically decaying correlation and the high temperature phase is totally disordered with exponentially decaying correlation. T_{KT} is proportional to the superfluid stiffness of the model. Thus, we identify T_c, the superconducting phase transition, with the phase ordering of the order parameter. It was pointed out by Emery and Kivelson that in the HTSC due to a combination of very low carrier density and high temperatures T_c is determined not by the pairing energy but by the energy scale of the phase fluctuation [9].

1.2.2   Relation between T_g and J_t

In an Hamiltonian of the form $J_t \sum_{<ij>} S_i S_j$, on an isotropic 3D lattice, it is quite clear that the transition into an AF ordered state is determined by J_t. The cuprates are anisotropic, and one can define the in-plane exchange constant which we identify with J_t, and an intraplane exchange $J_\perp$, in general $J_t >> J_{perp}$. It raises the question whether T_N is still set by J_t. As the temperature is lowered, the 2D planes develop AF correlations with a characteristic coherence length $\xi = C \exp(2J_t/kT)$. Thus, the effective interaction between the planes can be written as : $J_\perp \xi^2 \sum S_i S_j$ where now the summation is over blocks of spins with size ξ^2. So, when the effective interaction $J_\perp \xi^2$ equals J_t, the system is 3D like and orders. This happens at

$$kT_N = 4J_t / \ln(4J_t/J_\perp) \tag{1.1}$$

Therefore, we see that the anisotropy enters in T_N as a logarithmic correction. This can be seen in La_2CuO_4, where $J_t = 1540K$, $J_\perp/J_t = 5 \times 10^{-5}$ and $T_N = 315K$[10], which are of the same order of magnitude as the value we get using eq. 1.1.

As was shown in the previous sections, the cuprates show reminiscence of antiferromagnetic correlations even at optimal doping, and at low doping levels one can find frozen moments at low temperatures. The intuitive picture is of islands of hole-poor regions that have enhanced antiferromagnetism. These islands interact with each other very weakly, but eventually all the system freezes. This picture is illustrated in figure 1.3.

The effective interaction between the islands can be very complicated, but we argue that it is governed by the Heisnberg exchange constant J_t.

This argument can be supported by intuitive arguments. First, in analogy with melting experiments, we can think of a square lattice made of masses connected by
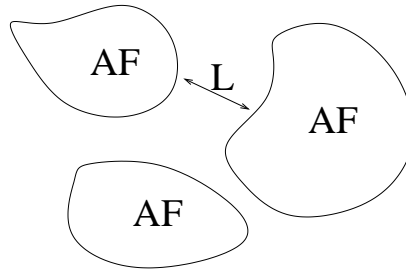
Figure 1.3: AF islands on a superconducting background.

איים אנטיפרומגנטים על רקע על-מוליך.

springs which their force constant is k. The melting temperature of this lattice is proportional to k. What happens if we now remove a percentage of the springs? The melting temperature is determined by the elastic constants which are a non-local, long wave length, property of the material. The rigidity of the lattice is a function of the local potential $\propto k$, and of the geometrical and topological configuration. When springs are removed the latter is changed, but the local energy scale stays the same. As a result, the melting temperature is still proportional to k, even if a substantial part of the springs is missing.

Various experiments and numerical calculations in La_2CuO_4 doped with Zn show that the Neel state survives up to doping levels of 40% which is the percolation threshold. Zn replaces a Cu ion in the planes, it has the same charge but has no spin, so doping with Zn is a way to dilute the lattice. In these experiments T_N decreases monotonously with doping up to a point where it vanishes. Neutrons experiments showed that the AF long range order exists in the CuO_2 planes up to the percolation point. An illustration of that point is given in figure 1.4.

The monotonic evolution of the average moment and of the Neel temperature as the doping is increased imply that no new energy scales are involved in this process,
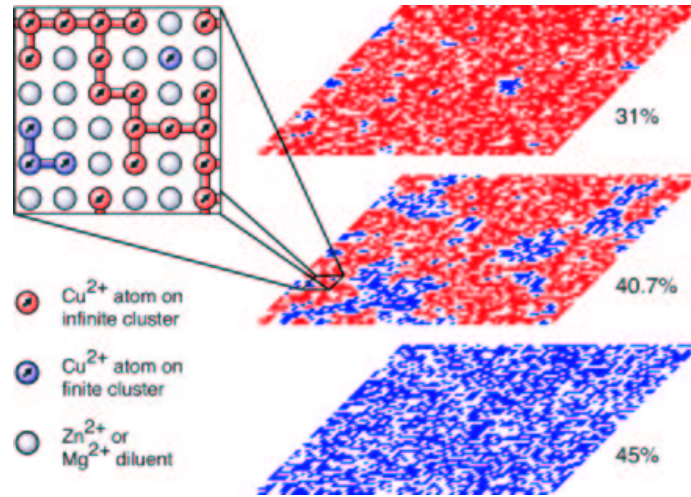
Figure 1.4: Spin configuration of $La_2Zn_xCu_{1-x}O_4$ as function of Zn doping level. Taken from [11]

קונפיגורציית הספין ב-$La_2Zn_xCu_{1-x}O_4$ כתלות ב רמת ה-Zn.

in that case the Neel temperature can be written as

$$T_N = Jf(x)$$

where J is the exchange interaction between spins, x is the dilution level. The function $f(x)$ depends on the dilution level and may depend on the configuration of the doping.

The behavior is totally different when La_2CuO_4 is doped with mobile holes. Doping with Sr puts holes in the CuO_2 planes and eliminates spins from them [12]. The magnetic phase digram of $La_{2-x}Sr_xCuO_4$ is shown in figure 1.5. What is seen clearly is that the mobile holes are much more effective in "killing" the AF state than the static holes. At $x \sim 0.02$ the long range order disappears, and instead a disordered ground state is found, this state is known as a cluster spin glass (CSG) [13, 14]. The short range AF order still exist in clusters, as was revealed by several experimental techniques [13, 15, 16].

In the region that interests us, the doping level is below percolation. The mobile
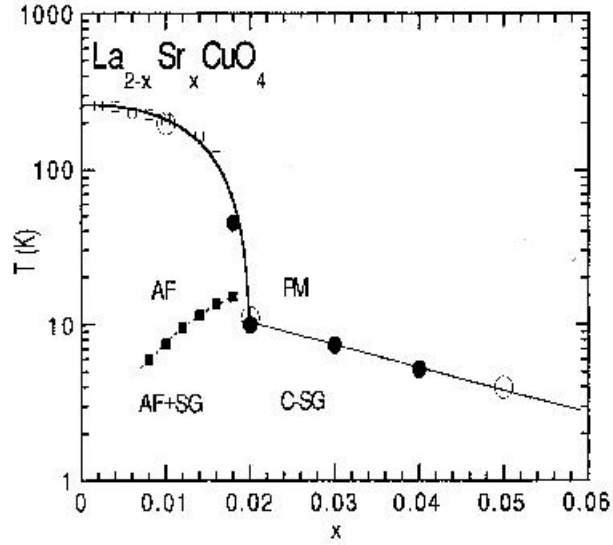
Figure 1.5: Magnetic phase diagram of LSCO
דיאגרמת פאזות מגנטית של $LSCO$

holes destroy the long range order by creating frustrated domain walls that move. If we could suddenly freeze the holes we would find an interconnected spin system, as we are below the percolation threshold. On this basis we assume that the relation $T_g \propto J_t f(x)$ still holds also where static long range AF order is missing.

1.3   The CaLaBaLaCuO system

$(Ca_x La_{1-x})(Ba_{1.75-x} La_{0.25+x}) Cu_3 O_y$ is a family of HTSC which belongs to the 1:2:3 system. It is tetragonal in all its range of existence $0 \le x \le 0.5$ [17]. If we compare it to the more famous YBaCuO system then Ca occupies the Y site, while La shares both the Y and Ba sites. This compound exhibits some interesting properties.

i) As the structure is tetragonal, there are no ordered CuO chains in the material, as found in most of the 1:2:3 compounds. The chains can complicate the interpretation
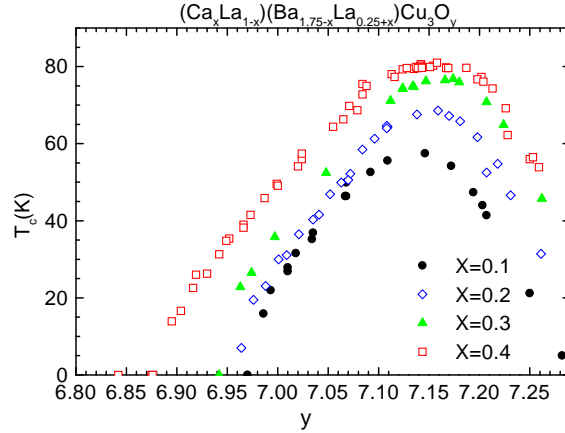
Figure 1.6: The variation of T_c with oxygen doping for various values of x. Taken from [43]

השינוי ב-T_c כתלות בריכוז החמצן עבור ערכים שונים של ריכוז ה-Ca.

of experiments.

ii) The CLaBaLaCuO is stable throughout all the parabolic T_c curve, meaning that by changing the O doping samples ranging from the underdoped to the overdoped can be synthesized, in contrast to most of the cuprates families that are stable only in part of the doping range.

iii) By changing x, parallel T_c vs O doping curves are formed, as can be seen in Fig 1.6. It is known from Bond Valence Sums (BVS) that the hole concentration in the CuO_2 planes does not depend on x [17]. As the mobile and chemical hole densities are believed to be related, T_c was expected to remain constant independently of x. Instead, as shown in Fig 1.6 the maximum value of T_c varies from $\sim 45K$ at $x = 0$ to $\sim 80K$ at $x = 0.4$.

The samples are prepared by a solid state reaction [17]. Essentially, raw powders are machine milled and baked in air at 950^oC for one day and re-grounded. This is

repeated 3 times. Then the powder is pressed into pellets, and the pellets are sintered for 70h in flowing oxygen at $960^{o}C$, and cooled at a rate of $10^{o}/h$. The desired oxygen content is achieved by oxygen reduction in a tube furnace in flowing oxygen at the right temperature. The reduction temperature determines the oxygen doping level in the material. After 24h in the furnace the samples are quenched in liquid N_2. For preparing overdoped samples the last step is done in high O pressure atmosphere.

After the preparation the samples are tested by X-ray to find spurious phases. We also characterize the samples by resistivity, ac and dc susceptibility. If the transition is found to be too broad, or two transition temperatures are found, the sample is regarded as a bad one. This compound has been prepared at our department for the last few years, so the preparation process was refined and by now it is very rare that a sample turns out to be bad. Furthermore, we have achieved very good control on the oxygen content of these samples, which is very important for our purpose, as the range of coexistence of magnetism and superconductivity is quite narrow.

The oxygen content is measured by iodometric titration, this method is capable of measuring y with an error of ± 0.001.

Chapter 2

EXPERIMENTAL METHODS

2.1 Muon Spin Relaxation (μSR)

μSR is a technique that allows sensitive studies of the magnetic properties of materials, by directly measuring the time dependence of the muon's spin, after injecting it into the sample. The method allows detection of static fields in the range of $10^{-5} - 1\text{Tesla}$, and of magnetic field fluctuations on a time scale of $10^{-3} - 10^{-11}$ sec.

2.1.1 Muon production, implantation and decay

The high intensities and flux needed to perform experiments in condensed matter are achieved using high energy proton beams produced in cyclotrons. The protons are fired into a target to produce pions via

$$p + p \rightarrow \pi^+ + p + n$$
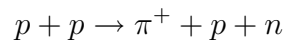
and the pions decay into muons:

$$\pi^+ \rightarrow \mu^+ + \nu_\mu$$
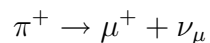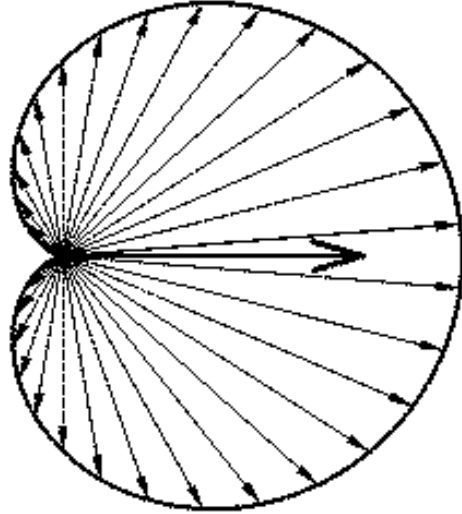
Figure 2.1: The angular distribution of emitted positrons with respect to the initial muon-spin direction. Taken form [18]

התפלגות זוויתית של הפוזיטרונים הנפלטים בתהליך הדעיכה של המיואון.

where ν_μ is a muon-neutrino. The pions that decay at the target surface, known as surface pions, have zero momentum, so the muon and the neutrino will have opposite momenta. The pion has no spin, thus by angular momentum conservation the muon and the neutrino have opposite spin. The neutrino's definite chirality ensures us that its spin is always aligned antiparallel to its momentum, and this implies that the muon spin is similarly aligned. In this way a beam of 100% spin polarized muons can be created. Muons hit the sample with an energy of 4MeV, they lose their energy very quickly by various scattering processes, common to all these processes is that their origin is Coulombic so they have no effect on the the muon's spin, and all the muons in the sample remain polarized in a certain direction.

The life time of the muon is $\tau_\mu = 2.2\mu s$, it decays in a three body process

$$\mu^+ \rightarrow e^+ + \nu_e + \bar{\nu_\mu}$$

This decay involves the weak interaction and it violates parity, this leads to the positron being emitted preferentially along the direction of the muons spin when it decayed. The angular distribution of the emitted positron is shown in figure 2.1. This effect allows one to follow the polarization of an ensemble of precessing muons. The positrons are detected using an array of plastic scintillators connected via a light-guide to a set of photo-multipliers.

2.1.2   Experimental setup and Data analysis.

Every muon implemented in the sample precesses according to the local magnetic field in its vicinity with an angular frequency given by $\omega = \gamma_\mu B$ where γ_μ, the gyromagnetic ratio, is 13.5 kHz/Gauss. Unlike other resonance techniques, no electromagnetic field is necessary, the detection of the precessing spin is done using the emitted positrons.

A schematic diagram of the experimental setup is shown in figure 2.2. In the simplest setup we have two detectors, the detector in the incident direction of the muons beam which is called the forward detector and the backward detector which is in the opposite direction. The histograms describing the number of positrons detected as function of time in the backward and forward detectors in a typical experiment are shown in figure 2.2. The number of positrons detected in all the detectors together decays exponentially with time, with a decay constant that is the lifetime of the muon. Thus the muon polarization can be extracted from the normalized difference between the histograms of the forward and backward detectors.

$$A(t) = \frac{N_B(t) - N_F(t)}{N_B(t) + N_F(t)}$$

$A(t)$ is known as the asymmetry plot, the maximal value of the asymmetry depends
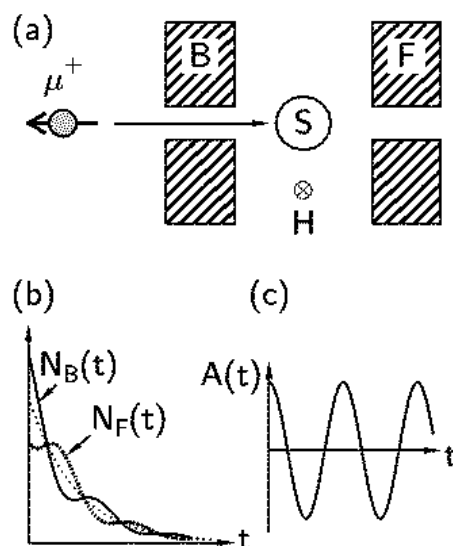
Figure 2.2: Schematic illustration of a μSR experiment. (a) the forward and backward detectors configuration. (b) The number of positrons detected in the forward and backward detectors as function of time. (c) The asymmetry function. Taken from [18]

איור סכמטי של ניסוי μ. (a) תצורת הגלאים. (b) מספר הפוזיטרונים שנקלטו בגלאי הקדמי והאחורי כתלות בזמן. (c) פונקציית האסימטריה של המיואון.

on the exact structure of the detectors system and on the intrinsic asymmetry of the positron decay and usually it is around 0.25.

μSR can be performed with no external field or with either a transverse or longitudinal field with respect to the initial muons spin direction. In the first case the muons will precess and reveal the internal field distribution, this is known as Zero Field μSR (ZF-μSR) and it is useful in research of ferromagnets, anti-ferromagnets and spin-glasses.

The case were the field is applied perpendicular to the initial muon spin direction (TF-μSR), causes the muon in the applied field. Any inhomogeneity in the field inside the sample or spin-spin relaxation (T_2 processes) will lead to dephasing and to decay

of the oscillating signal. In this method one can, for example, measure the penetration depth of the external magnetic field into a superconductor, as will be explained later on.

The third case, longitudinal field μSR (LF-μSR) is useful for measuring spin-lattice relaxation times (T_1) and more important to our case for distinguishing between static and dynamic relaxation in ZF-μSR, as will be explained later on.

Our μSR experiments were carried out at two facilities, ISIS at the Rutherford Appelton Laboratory in the UK and Paul Scherrer Institute in Switzerland. The difference between these two facilities is the time structure of the muons beam.

The PSI source is continuous, muons arrive to the sample one at a time. When a muon arrives it is detected by a muons detector that starts a clock, the clock is stopped when a positron hits the forward or backward detectors. This method allows very good time resolution that is essential for fast relaxing samples and for working in high fields at TF-μSR. We made our penetration depth measurements at PSI. The drawbacks of this method are complications that arise from a muon arriving to the sample before the first muon decayed, in that case there is no way to associate the positrons to specific muons and the events must be thrown away. This limits the maximal time for which the polarization of the muons can be traced to about $10\mu s$, which, as will be shown, is not enough for our ZF measurements. Another drawback is the relatively high background. The origin of the background is positrons that contaminate the muons beam (coming from muons that decayed on their way from the muons production target to the sample), these positrons hit the detectors and stop the clock, giving a constant background in the asymmetry plot, which can complicate the analysis of the ZF-μSR data.

The ISIS source is a pulsed source. In this case a large number of muons are
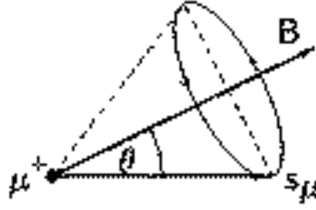
Figure 2.3: Muon spin precession about a magnetic field at an angle θ

פרסציה של ספין המיואון סביב שדה מגנטי בזווית θ.

implemented in the sample at once, then the clock is started. Every positron hitting the detectors is counted and its time of arrival relative to the pulse implantation time is recorded. In this way the two muons event problem is overcome and also the background problem does not exist because in between pulses the sample is separated from the muons source. The fact that the polarization can be traced up to times of 20μs combined with the absence of background signal makes ISIS more suitable for our ZF experiments. The problems with this method arise from the finite width of the muons pulse which results in a less accurate timing that limits the maximal precession frequencies that can be measured.

2.1.3   Static and dynamic relaxation

If the local magnetic field in the muon site makes an angle θ with the initial muon-spin direction, then the muon-spin will precess around the end of a cone of semi-angle θ about the magnetic field as shown in Fig 2.3. The polarization in the z direction will be:

$$P_z(t) = cos^2\theta + sin^2\theta cos(\gamma_\mu Bt)$$

Now, if we deal with a powder we should average over all possible field directions, this will lead to:

$$P_z(t) = \frac{1}{3} + \frac{2}{3}cos(\gamma_\mu Bt)$$

The origin of the constant 1/3 term is in sites in which the internal magnetic field is parallel to the initial muon-spin direction. Usually the internal field is not homogeneous, then one should also integrate over the field distribution, a famous example is the polarization line in a sample in which the internal field is distributed as a Gaussian of width Δ/γ_μ centered around zero, then the polarization is:

$$P_z(t) = \frac{1}{3} + \frac{2}{3}e^{-\Delta^2 t^2/2}(1 - \Delta^2 t^2)$$

a polarization known as the Kubo-Toyabe polarization, and shown in Fig 2.4. This was experimentally found in many samples when the origin of the internal field is frozen nuclear magnetic moments.

If the distribution were different, then the polarization line shape would be different, the common feature for all relaxation lines that originate in a static field distribution is the 1/3 term.

The muon can also lose its polarization due to dynamic fluctuations of the internal field, or if the muon hops from site to site. The effect of the hopping rate on the polarization is shown in Fig 2.5, it is assumed that the internal distribution is Gaussian. For fast hopping or fluctuations we get exponential relaxation, the faster the hopping the slower is the relaxation. This effect is an analog to the motional narrowing of NMR, the field is fluctuating so fast that in the time scale of the muon it is averaged to zero.

Slow fluctuations have very little effect on the polarization line shape at short times, but they will cause the 1/3 tail to relax. This allows sensitivity to very slow
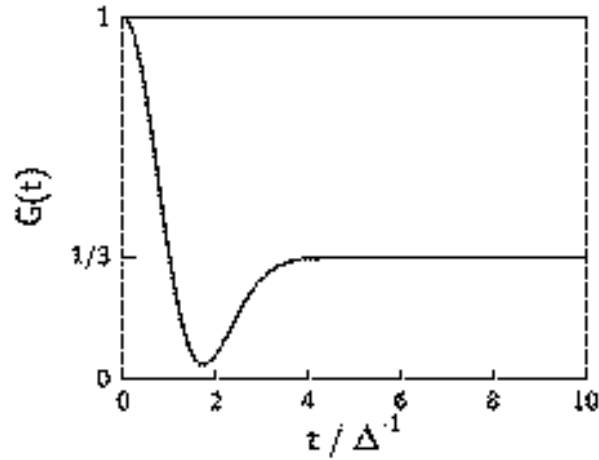
Figure 2.4: The relaxation of the muon-spin due to a Gaussian field distribution. Δ is the width of the distribution

דעיכת הקיטוב של ספין המיואון כתוצאה מהתפלגות גאוסית של השדה הפנימי בדגם.

dynamical fluctuations.

In some cases it can be difficult to distinguish between static and dynamic relaxation. A longitudinal magnetic field will have a large effect on the static part of the muon relaxation and a smaller effect on the dynamic part. The total filed experienced by the muon is a vector sum of the external and internal fields. As the external field is increased, the combined field is almost parallel to the initial polarization and the relaxation decreases. On the other hand, the fact that the external field changes the field distribution has no effect on the relaxation due to hoping between sites or fluctuations, as long as the field is not too high.

2.1.4   Measuring the penetration depth using muons

TF μSR is used to measure λ, the penetration depth of the external magnetic field. Since the muons probe the bulk of the sample and not the surface, the measurements
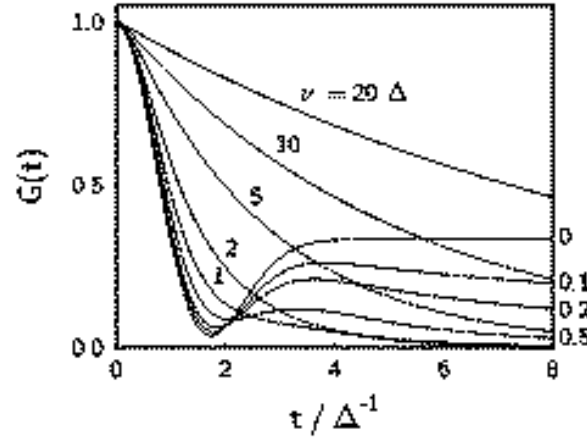
Figure 2.5: The relaxation function for a muon hopping at rate ν. The internal field is Gaussian distributed.

השפעת קצב קפיצת המיואון על דעיכת הקיטוב.

are done in the mixed state of the superconductor. In any type II superconductor two magnetic phases exist. Below the lower critical field H_{c1} the field penetrates to a thin layer on the surface of the sample, with a characteristic depth λ. Above H_{c1} the material is in the mixed state, in this phase magnetic flux is allowed to penetrate the bulk of the sample, but only in a form of flux vortices. The radius of the core of the flux vortex is defined by the coherence length of the superconductor ξ. The superconducting macroscopic wave-function is totally suppressed in the vortex core. The supercurrent screens the magnetic field over a length scale of the penetration depth λ.

For high enough fields the separation between vortices is smaller than λ, so the flux lines overlap. The muons implanted in the sample probe the distribution of the internal fields. This distribution leads to a damping of the muon spin precession

signal. The second moment of the distribution is proportional to λ^{-2} [19]

$$\sqrt{< \Delta B^2 >} \propto \frac{1}{\lambda^2} \tag{2.1}$$

For anisotropic superconductors, like the the high-T_c cuprates, the effective screening of the magnetic filed parallel and perpendicular to the CuO_2 planes is different, so it is possible to define a penetration depth λ_{ab} on the plane and λ_c in the c axis direction. In such materials $< \Delta B^2 >$ depends on the orientation of the crystal relative to the magnetic field, but for powders of highly anisotropic materials the second moment of the magnetic field distribution is given by [19]

$$< \Delta B^2 >= \frac{0.00371 F \Phi_0^2}{\lambda_{ab}^4} \tag{2.2}$$

where $F \sim 0.44$ for $\lambda_c/\lambda_{ab} \geq 5$ and Φ_0 is the fundamental flux quanta.

2.2 Magnetization measurements

2.2.1 Moving sample magnetometer

Let us consider a cylindrical sample of radius r and length L which moves through a coil from its upper part to its lower part and back. The dimensions of the coil are the same as the ones of the sample, and it has n turns per unit length. As the sample moves a distance dx in the coil, the field in a volume $\pi r^2 dx$ changes from H, the external field, to $B = H + 4\pi M$, where M is the sample magnetization. The change in the flux is $d\phi = n(\pi r^2)4\pi M dx$, therefore the voltage that develops in the coil is:

$$\epsilon(t) = -\frac{1}{c}\frac{d\phi}{dt} = \frac{1}{c}n(\pi r^2)4\pi M \frac{dx}{dt}$$

, where c is the speed of light. The output voltage will be proportional to the sample velocity and to its magnetization.

Now lets define $S = \int T_0 |\epsilon(t)| dt$ so that

$$S = [\int_0^{T/4} \epsilon(t) dt - \int_{T/4}^{T/2} \epsilon(t) dt + \int_{T/2}^{3T/4} \epsilon(t) dt - \int_{3T/4}^{T} \epsilon(t) dt]$$

where T is the period of the motion. Using the definition of ϵ, S is also given by

$$S = \frac{1}{c}(\phi(T/4) - \phi(0) - \phi(T/2) + \phi(T/4) + \phi(3T/4) - \phi(T/2) - \phi(T) + \phi(3T/4))$$

At times $T/4$ and $3T/4$, when the sample is in the center of the coil:

$$\phi = nBV_{sample} + nH(V_{coil} - V_{sample})$$

At times 0, $T/2$ and T, when the sample is out of the coil, we get:

$$\phi = nH v_{coil}$$

So we get

$$S = \frac{16\pi}{c} nMV_{sample}$$

In this case the signal depends on the product of the magnetization and volume of the sample.

2.2.2 Measuring Volume Fraction (VF)

In the limit of $H \to 0$ the magnetization is given by $m = \chi H V_{sc}$ where V_{sc} is the volume of the superconducting sample, which could be different from the volume V obtained from mass/density. Since we use a superconducting magnet there is an uncertainty in the absolute value of the field of about 5 G. For that reason the magnetization is measured over a range of positive and negative fields, and from the linear slope of m vs. H the quantity χV_{sc} is extracted.
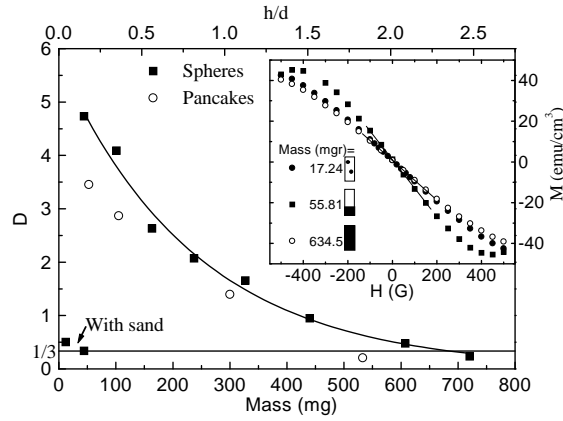
Figure 2.6: Superconducting volume of lead divided by the real volume vs. the mass of samples. In the top axis we show the dimensionality of the powder as the height it occupies in the sample container divided by its diameter. The solid squares represent sphere shaped grains and open circles represent pancake shaped grains. In the inset we show the magnetization curves for three characteristic cases described in the text.

הנפח העל-מוליך של עופרת לעומת נפח הדגם.

In order to obtain useful information from χV_{sc} we have to determine V_{sc} exactly. There are two definition of V_{sc}. The first is known as the shielding volume and is relevant in conditions of zero field cooling (ZFC). The second is the Meissner volume applicable in condition of field cooling (FC). In the FC case, the sample is heated to a temperature above T_c before the field is changed, and then cooled down in the new field. In powder samples, the ZFC leads to an overestimate of V_{sc} because in certain geometries Josephson connections can lead to shielding currents enclosing non-superconducting regions in the sample. The FC conditions, on the other hand, could lead to an underestimate of V_{sc} due to flux pinning in the sample.

In order to determine the correct V_{sc} we performed a preliminary experiment with Pb (Lead) spheres, each of diameter of 0.5mm. Pb is a type I superconductor, so λ is negligible. The measurements were done in FC conditions. We assume that χ is

the susceptibility of a single sphere including the demagnetization factor (-3/2) and obtained V_{sc}. We calibrated the susceptometer using a few spheres mixed with sand so that they are very well separated from each other. Raw data is presented in the insert of Fig. 2.6 where we show curves of $M = m/V$ vs H for 3 samples: (I) the few Pb spheres mixed with sand (17.24mg), (II) a layer of Pb spheres (55.81mg), and (III) a full container of Pb spheres (634.5mg). An artistic image of this experimental situation is also shown in the figure. In the first and third cases we find the same slope at $H \to 0$. But both are different from the second case. This means that isolated spheres and a full container of spheres give the same results. Our findings in terms of $f = V_{sc}/V$ are summarized in Fig. 2.6, where f is depicted as a function of sample mass, and as a function of height of spheres in the container (h) over its diameter (d), on the lower and upper abscissa, respectively. For a small number of Pb spheres, which form a 2D layer at the bottom of the container ($h/d < 1$), we find $f > 1$. As the number of spheres increases, the volume they occupy in the container becomes 3D in nature ($h/d > 1$), and f converges to 1. We repeated the experiment with "pancake" shaped pieces of lead; the results are qualitatively the same. This leads to one of the important findings of this work. As long as we are in FC conditions and use large values of h/d, we can safely assume that $V_{sc} = V$. This means that the magnetic field wanders inside the sample, in between the different grains, and fills all the empty spaces.

We performed two tests on a CLBLCO sample in order to demonstrate that the conclusions reached with Pb are applicable for these cuprates. However, here we reverse the role of the known and unknown parameters. We take $V_{sc} = V$ and determine χ from the measurements of the magnetization m. First, we repeated the susceptibility measurements as a function of mass for a CLBLCO sample with
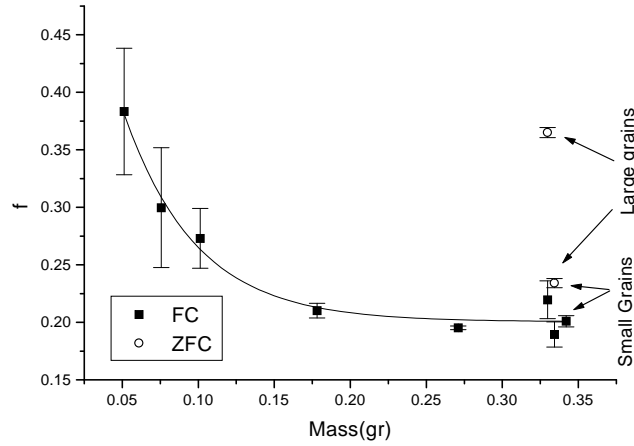
Figure 2.7: χ vs mass for a CLBLCO sample with $T_c = 42.3$ K. In addition we show χ as measured, both in FC and ZFC conditions, for two samples with different grain sizes. In the inset we show the magnetization curves for two grain sizes both in ZFC and in FC.

ראשיות מגנטית כתלות במסה עבור דגם של $CLBLCO$ בעל $T_c = 42.3K$.

T_c=42.3K. Here again a large mass means a 3D like sample. As can be seen in Fig. 2.7 the results are similar to those of the Pb powder in the sense that χ decreases with increasing mass and saturates. We interpret this as reaching the limit where the field wanders in between the grains, and conclude that in order to determine χ correctly we must work with a large enough mass.

Second, due to the combination of weak flux pinning (compared to low T_c super-conductors) and high temperatures, the time dependence of the magnetization can be very complex. It is known that the magnetization relaxes with time through a variety of mechanisms including flux creep, flux tunneling etc. Our main interest here is to find the optimal field cooling scheme, in order to get reproducible magnetization at base temperatures. We checked the susceptibility of a sample as a function of the cooling rate. We found, in agreement with previous works [20], that in FC conditions

it is important to pass through T_c slowly. Therefore, in all our measurements we cool the samples slowly enough so that no difference in the measurements is observed by cooling them even more slowly.

Having done all these tests we believe that we are on the safe side and our measurement indeed represents the true superconducting volume fraction of the samples.

Chapter 3

RESULTS

Our μSR experiments were done at two facilities. When a good determination of the base line was needed we used the ISIS pulsed muon facility at Rutherford Appleton Laboratory, UK. When high timing resolution was required we worked at the Paul Scherrer Institute, Switzerland (PSI).

Most of the data was taken with a ^{4}He cryostat. However, in order to study the internal field profile we had to avoid dynamical fluctuations by freezing the moments completely. For this purpose we used the ^{3}He cryostat at ISIS with a base temperature of 350 mK. All μSR measurements were done on sintered pellets.

3.1 ZF-μSR

Typical muon asymmetry depolarization curves are shown in Fig. 3.1 (a) for different temperatures in the $x = 0.1$ and $y = 7.012$ ($T_c = 33.1K$) sample. The change of the polarization shape with temperature indicates a freezing process, and the data can be divided into three temperature regions. In region (I), given by $T \geq 8$ K, the muon
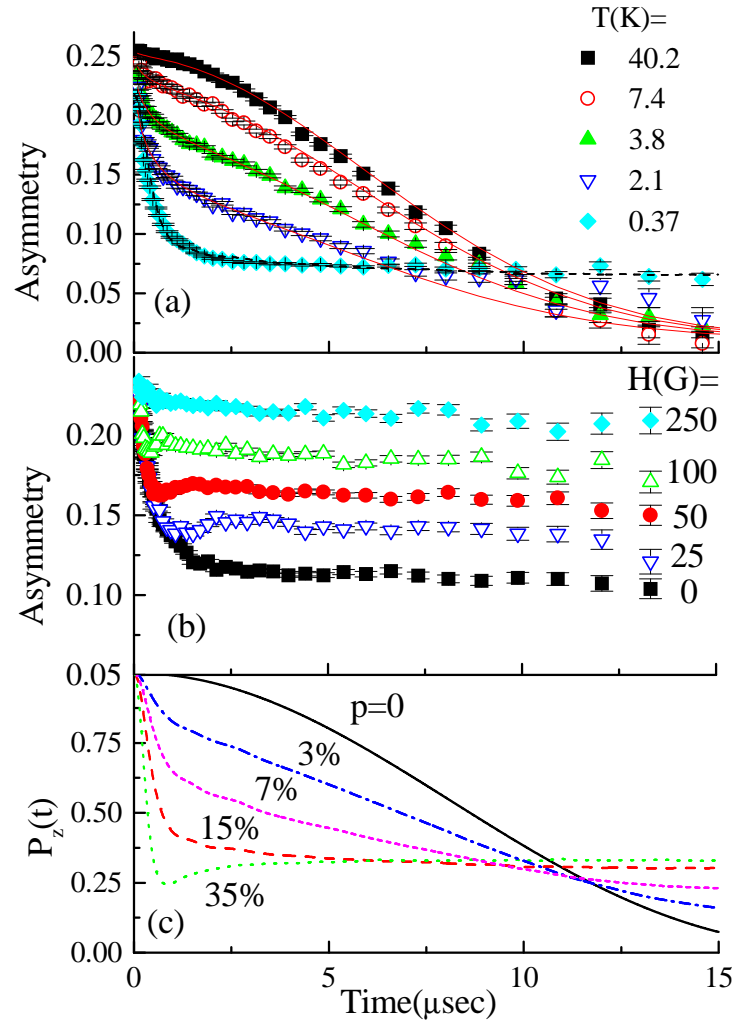
Figure 3.1: Typical assymetry plot for a CLBLCO sample with $T_c = 33.1K$. (a) Assymetry for various temperatures. (b) Assymetry as function of external longitudinal field. (c) Simulation results for various magnetic centers concentration (see text for details).

צורה טיפוסית של האסימטריה של המיואון בדגם של $CLBLCO$ עבור (a) טמפרטורות שונות. (b) שדות מגנטיים שונים.

relaxes according to the well known Kubo-Toyabe (KT) function given by

$$KT(t) = \frac{1}{3} + \frac{2}{3}(1 - \Delta^2 t^2)\exp(-\frac{1}{2}\Delta^2 t^2), \tag{3.1}$$

(see section 2.1.3) typical of the case where only frozen nuclear moments are present [21]. In region (II), bounded by $8\,\text{K} \geq T \geq 3\,\text{K}$, part of the polarization relaxes quickly and the rest relaxes as in the first region. As the temperature is lowered the rapidly relaxing part increases at the expense of the slow part. Moreover, the relaxation rate in the rapidly relaxing part seems independent of temperature. Finally, at long times the asymmetry relaxes to zero. In region (III), where $3\,\text{K} \geq T$, the asymmetry at long times no longer relaxes to zero, but instead recovers to a finite value. This value is $\simeq 1/3$ of the initial asymmetry $A_z(0)$. To demonstrate that the internal field is static at base temperature, the muon polarization was measured with an external field applied parallel to the initial muon spin-polarization. This geometry allows one to distinguish between dynamic and static internal fields. In the dynamic case the asymmetry is field independent [22]. In contrast, in the static case the total field experienced by the muon is a vector sum of H and the internal fields, which are of order $\langle B^2 \rangle^{1/2}$. For $H \gg \langle B^2 \rangle^{1/2}$ the total field is nearly parallel to the polarization. Therefore, in the static case, as H increases, the depolarization decreases, and the asymmetry recovers to its initial value. Because we are dealing with a superconductor, this field sweep was done in field-cooled conditions. Every time the field was changed, the sample was heated to above T_c and cooled down in a new field. The results are shown in Fig. 3.1 (b). In an external field of 250 G, the total asymmetry is nearly recovered. Considering the fact that the internal field is smaller than the external one due to the Meissner effect, this recovery indicates that the internal field is static and of the order of tens of Gauss. Next we perform quantitative data analysis in two

parts: high temperatures (region II), and base temperature.

3.1.1   High T Data Analysis

First we discuss region II. Here we focus on the determination of T_g. For that purpose we fit a combination of a rapidly relaxing function and a KT function to the data

$$A_z(t) = A_m \exp\left(-\sqrt{\lambda t}\right) + A_n KT(t), \tag{3.2}$$

where A_m denotes the amplitude of the magnetic part, λ is the relaxation rate of the magnetic part, and A_n is the amplitude of the nuclear part. The relaxation rate of the KT part was determined at high temperatures and is assumed to be temperature independent. Moreover,it is found to be almost the same for the samples we checked. The sum $A_m + A_n$ is constrained to be equal to the total initial asymmetry at high temperatures. The relaxation rate λ is common to all temperatures. The solid lines in Fig. 3.1 (a) are the fits to the data using Eq. 3.2.

The success of this fit indicates the simultaneous presence of two phases in the sample; part of the muons probe the magnetic phase while others probe only nuclear moments. As the temperature decreases A_m, which is shown in Fig. 3.2 for three samples, grows at the expense of A_n. At low temperatures A_m saturates to the full muon asymmetry. A similar temperature dependence of A_m is found in all our samples. The origin of the magnetic phase is electronic moments that slow down and freeze in a random orientation. The fact that λ is temperature independent means that in the magnetic phase $\gamma_\mu \langle B^2 \rangle^{1/2}$, where γ_μ is the muon gyromagnetic ratio, is temperature independent. In other words, as the temperature is lowered, more and more parts of the sample become magnetic, but the moments in these parts saturate upon freezing.
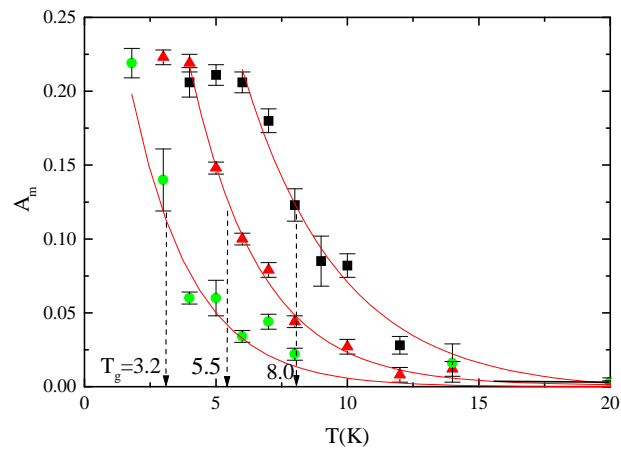
Figure 3.2: Magnetic amplitude as function of temperature for different samples. The solid lines are guides to the eye.

משרעת החלק המגנטי של הרלקססיה כתלות בטמפרטורה.
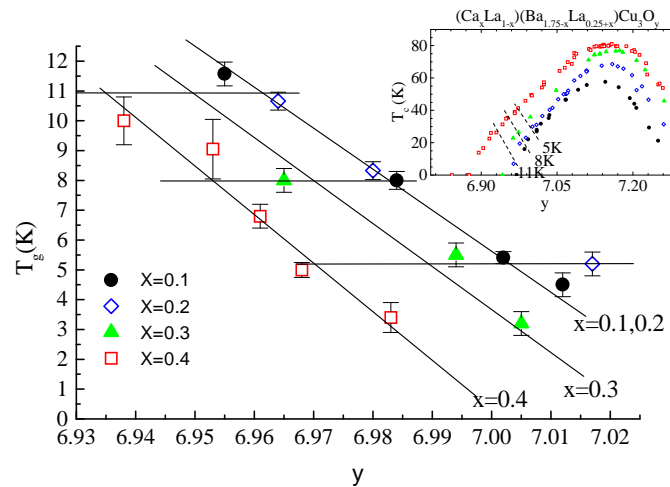
Figure 3.3: T_g vs. y. The horizontal solid lines are the equal T_g lines appearing in the insert.

דיאגרמת הפאזות המגנטית. T_g כתלות ב y עבור ערכי x שונים.

Our criterion for T_g is the temperature at which A_m is half of the total muon polarization as demonstrated by the vertical lines in Fig. 3.2 for three different samples. The phase diagram that is shown in Fig. 3.3 represents T_g for various samples differing in Ca and O contents. This diagram is systematic and rather smooth suggesting good control of sample preparation. As expected, for constant x, higher doping gives lower T_g.

We have singled out three groups of samples with a common $T_g = 11$, 8 and 5 K as shown in Fig. 3.3 by the horizontal solid lines. These samples are represented in the phase diagram in the inset of figure 3.3 by the dotted lines.

3.1.2 Low T Data Analysis

We now turn to discuss the muon depolarization at base temperature. In this case all the muons experience only a static magnetic field, as proven above. This allows one to reconstruct the internal field distribution out of the polarization curve. The polarization of a muon spin experiencing a unique field $\mathbf{B}$ is given by $P_z(t) = \cos^2(\theta) + \sin^2(\theta)\cos(\gamma|\mathbf{B}|t)$, where θ is the angle between the field and the initial spin direction. When there is an isotropic distribution of fields, a 3D powder averaging leads to

$$P_z(t) = \frac{1}{3} + \frac{2}{3}\int_0^\infty \rho(|B|)\cos(\gamma|B|t)B^2 dB \tag{3.3}$$

where $\rho(|B|)$ is the distribution of $|\mathbf{B}|$. Therefore, the polarization is given by the Fourier transform of $\rho(|B|)B^2$ and has a 1/3 base line. When the distribution of $\mathbf{B}$ is centered around zero field, $\rho(|B|)B^2$ is a function with a peak at $\langle B \rangle$ and a width Δ [e.g. Fig 3.4(b)]. Therefore we expect the polarization to have a damped oscillation and to recover to 1/3, a phenomenon known as the dip [e.g. the inset in Fig 3.4 (b)]. Gaussian, Lorentzian and even exponential random field distributions [23], and,

more importantly, all known canonical spin glasses, produce polarization curves that have a dip before the 1/3 recovery. This is demonstrated in Fig. 3.5. For a Gaussian distribution of width Δ we obtain Eq. 3.3 which is demonstrated in panel (a). The cases of a canonical spin glass $Fe_{0.05}TiS_2$, and an extremely underdoped CLBLCO are presented in panels (b) and (c). Furthermore, a dipless polarization curve that saturates to 1/3 cannot be explained using dynamical arguments. Therefore, the most outstanding feature of the muon polarization curve at base temperature is the fact that no dip is present, although there is a 1/3 tail. This behavior was found in all of our samples with $T_c > 7$ K, and also in Ca doped YBCO [24] and Li doped YBCO [25].

The lack of the dip in $P_z(t)$ can tell much about the internal field distribution. It means that $\langle B \rangle$ is much smaller than Δ. In that case the oscillations will be over-damped and the polarization dipless! In Fig. 3.4 we show, in addition to the $\langle B \rangle \simeq \Delta$ case described above [panel (b)], a field distribution that peaks around zero [panel (a)]. Here $\langle B \rangle$ is smaller than Δ, and, indeed, the associated polarization in the inset is dipless. Thus in order to fit the base temperature polarization curve we should look for $\rho(|B|)B^2$ with most of its weight around zero field. This means that $\rho(|B|)$ diverges like $1/B^2$ at $|B| \to 0$, namely, there is an abnormally high number of low field sites.

It also means that the phase separation is not a macroscopic one. If it were, all muons in the field free part would probe only nuclear moments and their polarization curve should exhibit a dip or at least its beginning, as in the high temperature data. The same would apply for the total polarization curve, in contrast to observation. Thus, the superconducting and magnetic regions are intercalated on a microscopic scale ($\sim 20\mathring{A}$) [26]. This is the third main finding of this work.
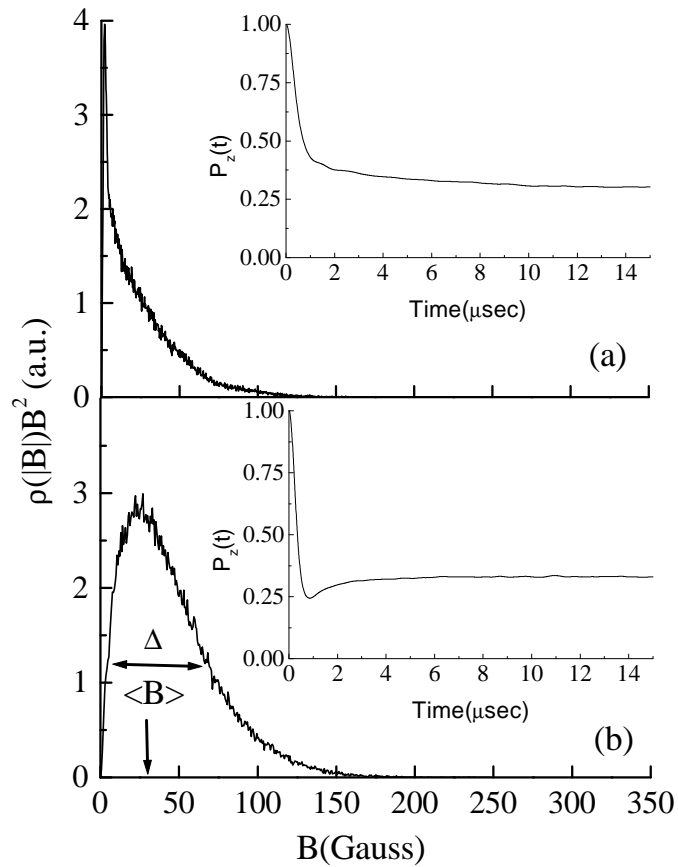
Figure 3.4: (a) The internal field distribution extracted from the simulations for the case of correlation length $\xi = 3$ lattice constants, maximum moment size of $0.06\mu_B$ and magnetic moment concentration $p = 15\%$. Inset: The muon spin polarization for that distribution. (b) The same as above for the case of $p = 35\%$. For details see section 4.1

התפלגות השדה בדגם והאסימטריה של המיאון בהתפלגות כזו. ב-(a) התפלגות בה רוב המשקל בשדות נמוכים מאד. ב-(b) התפלגות גאוסית.
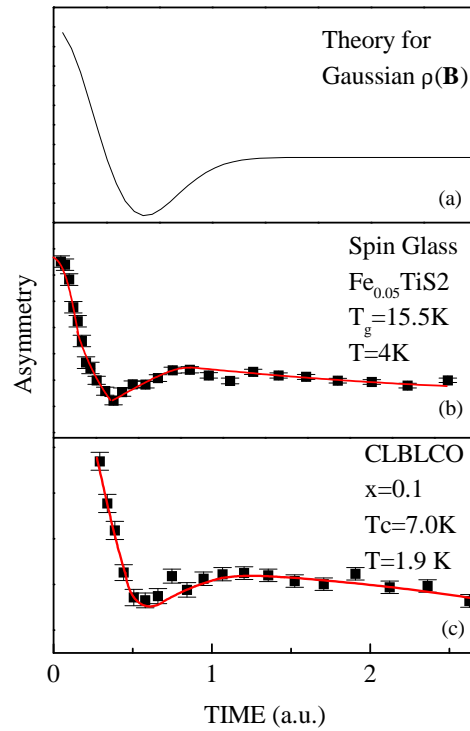
Figure 3.5: Demonstrating the expected muon spin polarization function for (a) a Gaussian field distribution, (b) in a canonical spin glass $Fe_{0.05}TiS_2$, and (c) extremely underdoped CLBLCO.

הדגמה של הרלקסציה של המיואון בהתפלגות גאוסית. (a)-ב. הפונקציה התאורטית. (b)-ב תוצאה ניסיונית עבור $Fe_{0.05}TiS_2$. (c)-ב תוצאה עבור דגם $CLBLCO$ בעל $T_c = 7K$.

The special internal field distribution, and the nature of the gradual freezing of the spins, can be explained by the intrinsic inhomogeneity of hole concentration. The part of the sample that is hole poor, and for that reason is "more" antiferromagnetic, will freeze, while the part which is hole rich will not freeze at all. The variation in the freezing temperature of different parts of the sample can be explained by the distribution of sizes and hole concentration in these antiferromagnetic islands [13]. The large number of low field sites is a result of the fact that the magnetic field generated in the magnetic regions will penetrate into the hole rich regions but not completely.

3.2   TF-μSR

We performed TF-μSR for two main reasons, to check that the CLBLCO system satisfies the Uemura relations and as a test of the quality of the samples. As explained in a previous section, using TF-μSR one can relate the magnetic penetration depth to the de-polarization rate of the muon. This method is based on the formation of a lattice of vortices in the sample, the measured penetration depth is an average over all the sample volume. Any macroscopic spurious phase will change the muons polarization and can be detected. We checked all our CLBLCO samples and all of them were found to be bulk superconductors.

These experiments are done by field cooling (FC) the sample to 1.8 K in an external field of 3 kOe in PSI and 400 Oe in ISIS. As explained above we apply the field perpendicular to the incoming muons spin direction, and every muon then precesses according to the local field in its environment. When field cooling the sample, a vortex lattice is formed, and the field from these vortices decays on a

length scale of λ. This leads to a inhomogeneous field distribution in the sample. Since the magnetic length scale is much larger than the atomic one, the muons probe the magnetic field distribution randomly, which, in turn, leads to a damping of the muons average spin polarization. This situation is demonstrated in Fig. 3.6 where we present an image of the field profile, and the corresponding real and imaginary parts of the muon asymmetry. At temperatures above T_c the field is homogeneous and all muons experience the same field, and therefore no relaxation is observed. Well below T_c there are strong field variations and therefore different muons precess with different frequencies, and the average polarization quickly decays to zero. In intermediate temperatures the field variations are not severe and the relaxation is moderate.

It was shown that in powder samples of HTSC the muon asymmetry $A(t)$ is well described by [21],

$$A(t) = A_0 \exp(-\sigma^2 t^2/2) \cos(\omega t + \varphi) \tag{3.4}$$

where A_0 is the initial asymmetry, $\omega = \gamma_\mu H$ is the precession frequency of the muon, σ is the relaxation rate, and φ is a phase which depends on the counters used to generate the asymmetry. Our analysis for both ISIS and PSI data is done in a reference frame rotating at ω_{rrf} and the real and imaginary components of the signal are fitted simultaneously. Therefore, the frequency in Fig. 3.6 is $\gamma_\mu H - \omega_{rrf}$ where ω_{rrf} is chosen arbitrarily for presentation purpose. The solid line in this figure is the fit result. The fact that the whole asymmetry relaxes indicates that CLBLCO is a bulk superconductor.

In figure 3.7 we show the variation of σ versus the temperature for two samples. In the upper panel the sample does not show signs of magnetism at low temperature, $\sigma(0)$ is taken as the value at the lowest temperature measured. On the other hand,
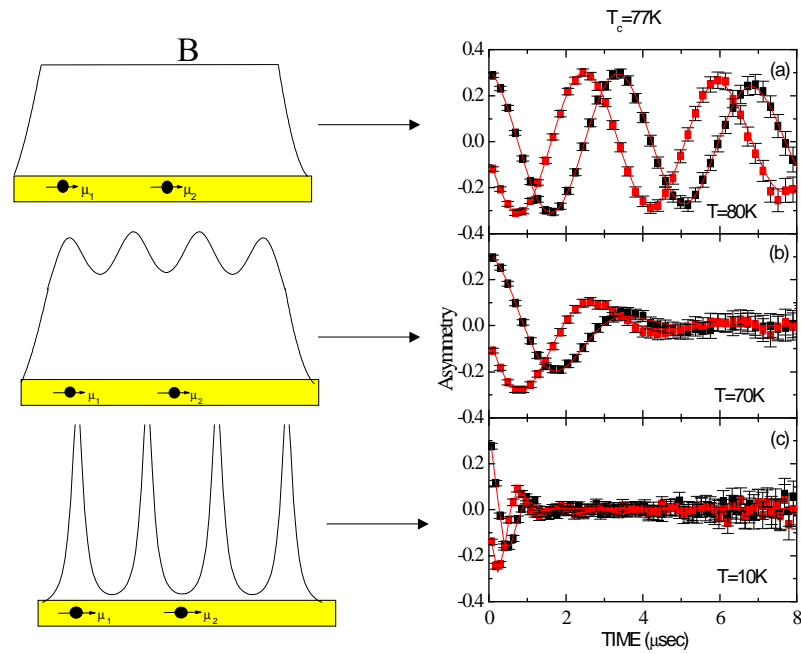
Figure 3.6: Demonstrating the relation between the field distribution and the real and imaginary asymmetries in a TF-μSR experiment. This data was taken at ISIS and is presented in a rotating reference frame.

הדגמה של הקשר בין התפלגות שדה ניצב בדגם לרלקסציה של תנודות ספין המיואון.
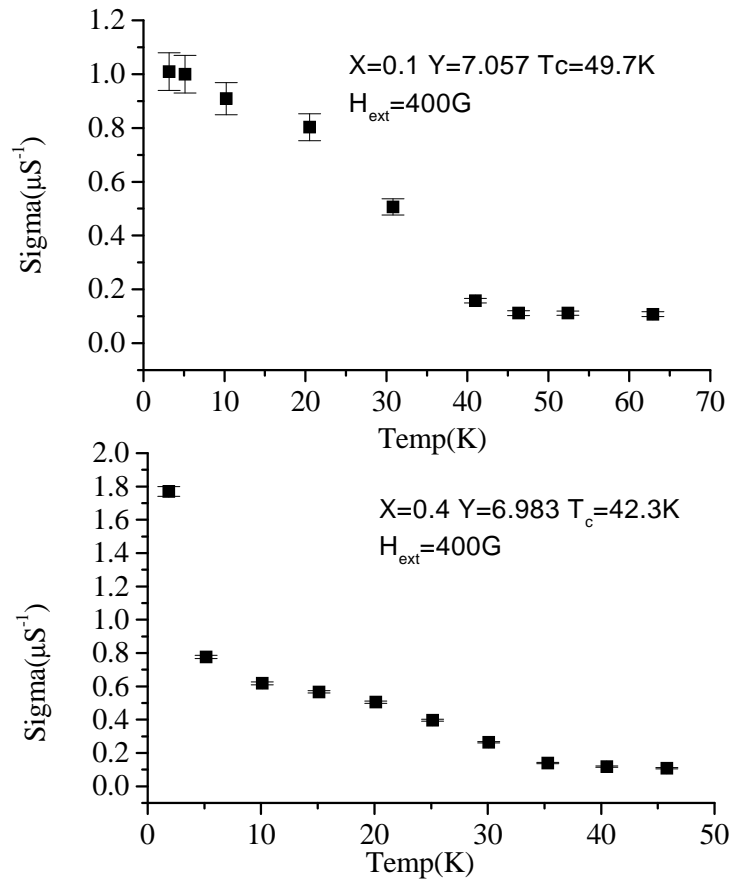
Figure 3.7: *sigma* the relaxation constant as function of temperature for two CLBLCO samples. In the upper panel a non-magnetic sample. In the lower panel an underdoped sample that shows magnetism at low temperatures.

קבוע הרלקסציה σ כתלות בטמפרטורה. עבור דגם לא מגנטי (חלק עליון) ודגם מגנטי (חלק תחתון).

in the lower panel there is a sudden increase in the relaxation at low temperatures due to the freezing of magnetic moments. In cases like that, typical to underdoped samples, we had to fit the σ vs T, excluding the very low temperature points, to a Gaussian to determine $\sigma(0)$. An important finding is that upon the appearance of the magnetism there was no change in A_0. This, again, indicates that the magnetic moments do not come from a separated macroscopic phase, the muons probe all the sample at all temperatures.

The fit results for σ are shown in Fig 3.8. As can be seen, the dependence of T_c on σ is linear in the under-doped region and universal for all CLBLCO families, as expected from the Uemura relations. However, there is a new aspect in this plot. There is no "boomerang" effect, namely, overdoped and underdoped samples with equal T_c have the same σ, with only slight deviations for the $x = 0.1$ sample as demonstrated by the arrows in Fig. 3.8. Therefore, in CLBLCO there is a one to one correspondence between T_c and σ, and therefore λ_{ab}^{-2}, over the whole doping range.

The penetration depth λ can be related via the London equation to the spuerfluid density n_s,

$$\lambda^2 = \frac{m_*}{n_s e^2} \tag{3.5}$$

The Uemura plot shows that T_c is linearly proportional to the superfluid density, at least in the underdoped regime. This result is totally unexpected in the BCS framework. In a BCS-like theory T_c is determined by the size of the energy gap which should depend, if at all, only weakly on the pair density.

An explanation to this phenomena was given by Emery and Kivelson, as was discussed in section 1.2.1.
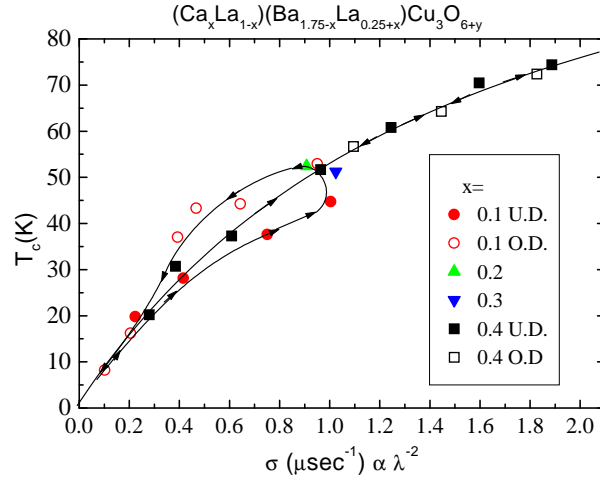
Figure 3.8: A Uemura plot showing T_c vs. the muon relaxation rate σ in Eq. 3.4 for the CLBLCO family of superconductors.

גרף $Uemura$ שמראה את קבוע הרלקסציה של המיואון, σ, כתלות ב-T_c. עבור משפחת ה-$CLBLCO$.

3.3   Magnetization measurements

We measured the magnetization of various families of HTSC, the YBCO, LSCO and CLBLCO systems. From these measurements we calculated the superconducting volume fraction (VF) as explained in section 2.2.2.

In Fig 3.9 we show the VF measured in FC conditions vs. y for various x values for CLBLCO samples, in the inset we show T_c vs y and x. The similarity between the two plots is obvious. Plotting the VF vs T_c reveals that they are indeed linearly dependent, at least in the underdoped regime, as shown in figure 3.10. The results for the LSCO and YBCO samples are the same, as seen in Fig 3.11. Not only do the different families show the same linear behavior, but also the slope of the VF vs T_c is the same! This is not a trivial result, taking into account that there are quite a few differences between the families and between the samples within every family. Let us
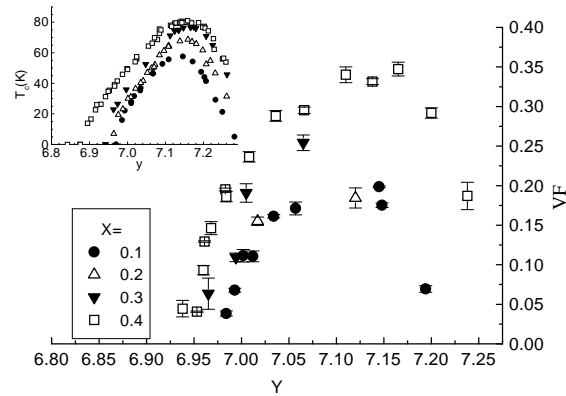
Figure 3.9: The VF as function of y for various values of x for many CLBLCO samples. In the insert we show T_c vs y for comparison.
.החלק העל-מוליך כתלות בריכוז החמצן עבור דיגמי $CLBLCO$
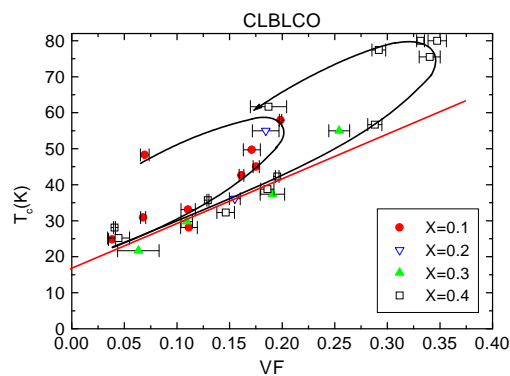
Figure 3.10: Vf vs. T_c for the CLBLCO system.
.$CLBLCO$-החלק העל-מוליך כתלות בטמפרטורת המעבר העל-מוליך עבור משפחת ה
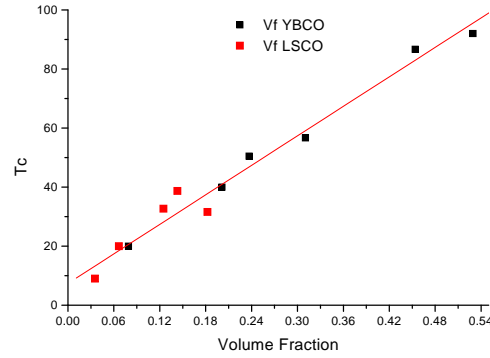
Figure 3.11: T_c versus the volume fraction of LSCO and YBCO samples.
T_c כתלות בחלק העל-מוליך עבור דגמים של $YBCO$ ו-$LSCO$.

summarize some of the relevant differences between them:

1. The CLBLCO samples are tetragonal at all doping levels, while the YBCO and LSCO, in the relevant temperature range, are orthorombic. This implies that in LSCO and YBCO twin boundaries exist in the sample, while in CLBLCO they don't.

2. The superconductivity in the YBCO family is more isotropic than in the LSCO family. The ratio $\frac{\lambda_c}{\lambda_{ab}}$, is much larger in LSCO than in YBCO, where λc is the magnetic penetration depth perpendicular to the CuO planes and λ_{ab} is the penetration in the plane [27]. This ratio in the CLBLCO system in not known but is expected to be similar to that of YBCO.

3. The YBCO and CLBLCO systems are double layer systems while LSCO is a single layer cuprate. By the layer number we mean the number of CuO_2 planes in a unit cell.

In order to better understand this result, one has to deal with the non trivial
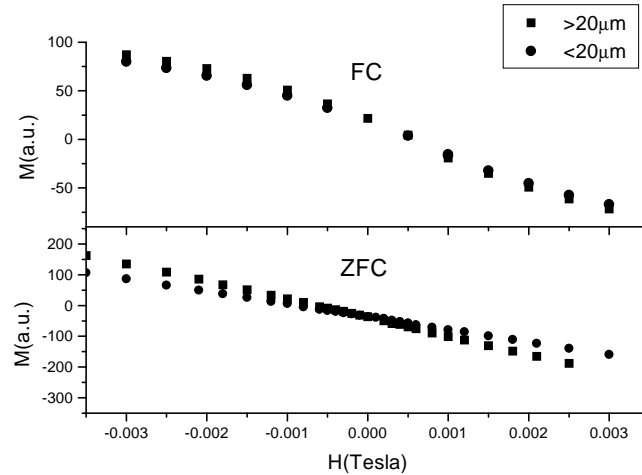
Figure 3.12: Magnetization vs. field for two powder samples with different grains size.

מגנטיזציה כתלות בשדה עבור שני אבקות $CLBLCO$ בעלות גודל גרגיר שונה.

subject of the magnetization of HTSC powders. We did few other experiments trying to gain some insight into this problem.

Using a set of sieves we divide one CLBLCO powder sample into two: $20\mu m < d < 40\mu m$ and $d < 20\mu m$ where d is the characteristic size of a grain. We measured the VF of these two samples both in ZFC and FC conditions. The results are shown in figure 3.12. First of all, one can see that in ZFC the magnetization is linear in the field up to a much higher field than in FC. In the example shown in Fig. 3.12 the ZFC data for both grain sizes is linear in all the range measured ($\sim$ 30 Gauss), while in the FC data it is hard to find any region in which the magnetization is linear in the field. In this case we define the VF using the region between -5Gauss and 10Gauss (The magnetization is not symmetric around zero field because of the superconducting magnet). This was found in all the samples, the linear region can be different between samples but it is always of the order of 10Gauss. We believe
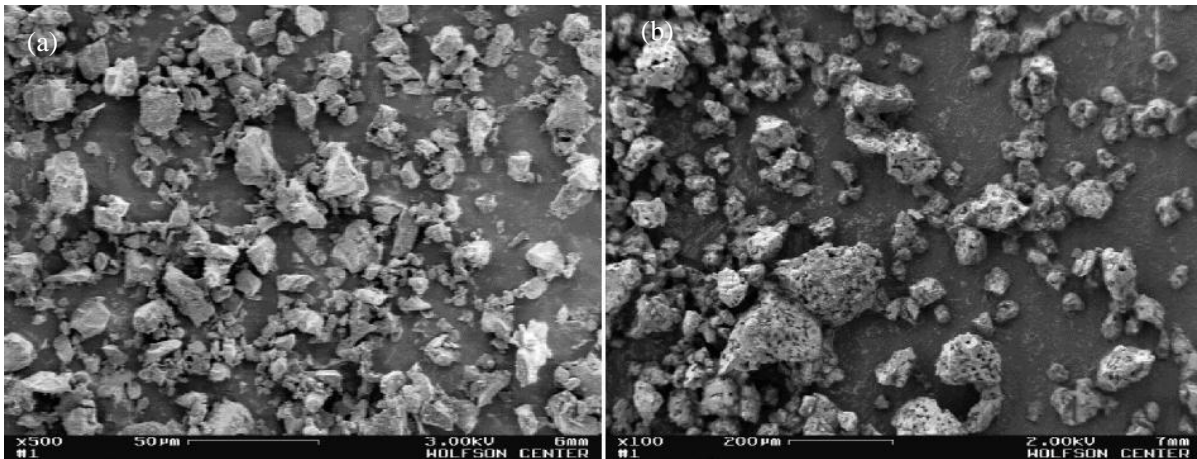
Figure 3.13: Scanning electron micrographs of the powder. (a) Small grains (b) Large grains.

תמונת מיקרופקופ אלקטרוני של שני גדלי אבקה של דגם $CLBLCO$.

the point where the linearity breaks down is the point at which flux pinning starts to occur, as will be discussed latter on.

Secondly, we find almost no grain size dependence in the FC measurements, especially when compared to the ZFC experiment. This indicates that the grain size does not play a role in determining the VF as long as FC conditions are used. This can be understood if one assumes that the powder grains are agglomerates of smaller crystallites. All our samples during their preparation are pressed and sintered into pellets, and then crashed back into powders. It is conceivable that the more the samples are crashed the more the basic crystallites are separated, but without a true change in the size of the basic building block of the sample.

The scanning electron micrographs (SEM) of the two samples support this picture, they are shown in figure 3.13. The large grains (panel b) look like they are made of smaller grains, they look much more porous than the small grains. The distribution of size of grains in both samples looks quite broad.
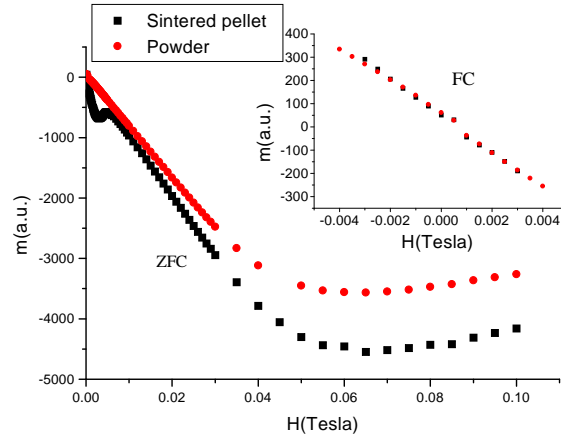
Figure 3.14: The magnetization vs. magnetic field of a LSCO sample with x=0.15. We show the FC and ZFC results for a sintered pellet and for the same sample after pulverization.

השוואת המגנטיזציה של דגם $LSCO$ במצב מסונטר ובמצב של אבקה.

We compared the magnetization of a whole pellet with its magnetization after crashing it. We used for this purpose a LSCO sample with $x = 0.15$ and $T_c \sim 40K$. The results are shown in figure 3.14. In the ZFC results one can see a great difference between the magnetization of the pellet and powder in low fields. While the powder shows the well known linear dependence on the field up to more than 150Gauss, the pellet magnetization does not show linear behavior at all. Up to 20Gauss the calculated VF is almost 100%. Above that field, the VF decreases and reaches a value similar to that of the powder. The difference between the two samples is only the connection between the grains, those can be described as Josephson junctions with some average critical field H_{Jc1}. At fields lower than H_{Jc1} in ZFC there are shielding currents that shield all the volume of the pellet. Above H_{Jc1} the links can not support the shielding current any more and we get local shielding as in the powder.

On the other hand, the FC magnetization of the pellet and of the powder are the

same. This difference between the ZF and ZFC behavior of the pellet indicates that the intergrain connections can not carry any Meissner currents but they can carry shielding currents.

The result is consistent with the existence of a basic building block for the samples. If we accept this picture, than there is no real difference between a pellet and a powder grain, they are both made from the same smaller cristallines. Thus, we see that in general the Meissner fraction of the superconducting grains is not complete. One of the reasons for that can be that the penetration depth in this materials is quite large.

It was shown that the magnetization of a SC grain neglecting demagnetization effects and pinning, depends on the ratio between the penetration depth λ and the typical length scale of the grain's cross section, a. χ can writen

$$\chi = -b(1 - g(x)/x) \tag{3.6}$$

where $x = a/\lambda$. In spherical, plane and cylindrical shaped grains $g(x)$ is the Langevin, Hyperbolic tangense and the modified Bessel functions respectively [28]. In the limiting cases all the above function have the same x dependence [28]. For the case $x >> 1$

$$\chi \propto -(1/4\pi)(1 - \lambda/a) \tag{3.7}$$

and for the case $x << 1$

$$\chi \propto -(1/4\pi)(a^2/\lambda^2) \tag{3.8}$$

We used the intrinsic anisotropy of the HTSC to check in which of these two limits our experiment lies, $x > 1$ or $x < 1$. Two samples of YBCO powder in glue are used. In one of the samples the powder is oriented and in the other it is not. In figure 3.15 we show the experiment in a schematic way. In panel a of the figure, the CuO_2 planes are oriented parallel to field and the penetration is in the c direction , in panel
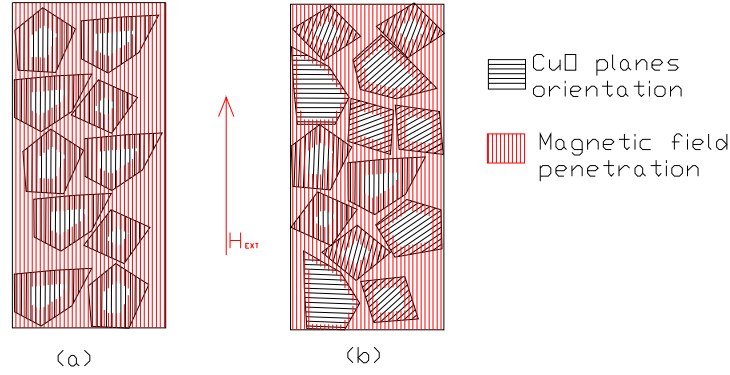
Figure 3.15: Schematic illustration of the dependence of VF on the orientation of the powder grains.

איור שמתאר את התלות של גודל החלק העל-מוליך בסדר הזוויתי של גרגירי האבקה.

b the orientation of the CuO_2 planes is random and so the penetration direction is random too. λ_c/λ_{ab} in YBCO is around 5 [27], so if the grain size is much larger than the average penetration length we expect no difference between the VF of the two samples, this is in contradiction to what was found in the experiment. The grains size according to this experiment is of the same order as the penetration length or smaller.

We fitted the VF data of the CLBLCO $x = 0.4$ samples to both equation 3.8 equation 3.7 using the λ values we got from the TF-μSR experiment. Both the models fit the data reasonably well, if we assume $a > \lambda$ we get for a a value of $\sim 2000\mathring{A}$. If we assume the opposite we get $a \sim 500\mathring{A}$. The fact is that in any case the size of the SC block is of the same order as the penetration depth.

Some authors tried to explain the incomplete Meissner fraction in the HTSC. Wohlleben *et. al.* [29] argued that in sintered pellets of HTSC there exist a critical field H_m above which the screening of magnetic fields out of the sample will not be

complete. This results from the intrinsic structure of these materials, which contains many extended defects, such as grain boundaries and twining planes, that are transparent to magnetic fields. The second condition for the incomplete shielding is that the characteristic distance between these defects, which defines the real superconducting block, will be such that it is much larger than λ_{ab} and smaller than λ_c. Under these conditions the maximal Meissner fraction of the pellet will be 1/3. Below H_m the Meissner fraction will rise to 100% in the presence of Josephson loops.

There are several crucial points in this model that don't agree with our data. First of all it is known, that at least in YBCO, the anisotropy in the penetration depth is no more than one order of magnitude. Thus, it is difficult to see how YBCO satisfies the conditions of the model. Second, in this model the incomplete Meissner fraction is an equilibrium property of granular HTSC, an idea which is hard to accept taking into account the differences between ZFC and FC measurements.

Two other models describe the incomplete Meissner fraction as a metastable state that depends on the history of the sample. The first is the glass superconductor model [30]. This model treats the granular superconductor as a random array of Josephson loops. We don't elaborate on this model because the main ingredient of it is the connection between the grains, which we believe is not relevant to our problem. This was shown by comparing the VF in FC of a pellet and of the powder produced by pulverizing the same pellet.

The second model explains the incomplete Meissner fraction by flux-pinning. A well know phenomenon in the HTSC is the irreversibility line which defines, for every applied field, a temperature above which the FC and ZFC magnetization are the same. The irreversibility line follows the relation

$$1 - t \propto H^{2/3}$$
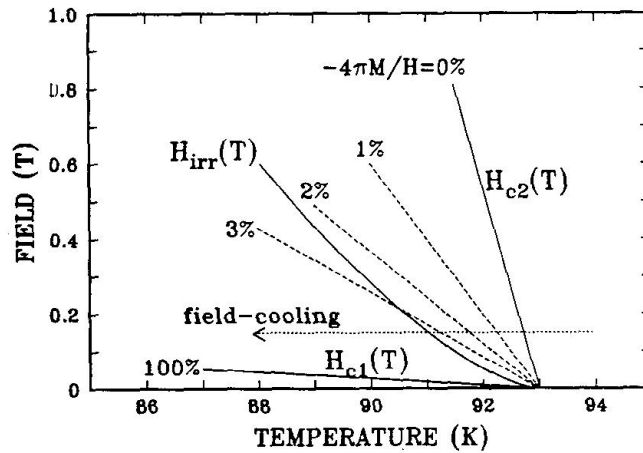
Figure 3.16: Critical fields and irreversibility line for an optimally doped YBCO
sample. The dashed lines represent lines of equal VF. Taken from [31]
שדות קריטיים וקו האי-הפיכות של דגם $YBCO$.

where t is the reduced temperature T/T_c. The irreversibility line was explained by
Yeshurun and Malozemoff as a result of conventional flux pinning and thermally
activated flux creep [31]. The irreversibility line leads to an incomplete Meissner
effect in FC. When the sample is cooled in a magnetic field, very close to T_c it will
be above the first critical field, H_{c1}, so the magnetization of the sample, M, will be
larger than $-H/4\pi$. As the sample is cooled further the field is expelled from the
sample until one reaches the irreversibility temperature of the specific field. Cooling
more will not change the magnetic moment of the sample. This is shown in figure
3.16. Although at base temperature all the measurements were taken at fields much
lower than H_{c1}, the magnetization is determined at much higher temperatures, where
the applied fields can form a flux lattice in the sample. On the other hand, if the
sample is cooled in zero field, then no flux is trapped inside. In this sense the model
can explain the difference between FC and ZFC measurements.

The main disagreement we find between this model and our data is the field

dependence of the Meissner fraction. As the irreversibility temperature depends on the external field, it is expected that there will be a substantial field dependence of the Meissner fraction, we on the other hand found no field dependence at all. To double check this point we measured one of our YBCO samples in a SQUID magnetometer (at the Weizmann institute) at low fields down to 0.1 Gauss with a resolution of 0.1 Gauss, we again found a linear magnetization with same slope we found using our own magnetometer.

The most problematic issue is more general and concerns pinning of flux in very small particles. The overall flux through a small grain with surface area S is $\phi = B \cdot S$. The flux quanta is $\phi_0 = 2 \times 10^{-7} Gausscm^2$, if the flux through the grain is less than half flux quanta it is energetically unfavorable for the system to pin flux in it. The condition for flux pinning is:

$$\frac{BS}{\phi_0} > 0.5$$

If we assume $S = 1\mu m^2$ (on the same order as the penetration depth) then the minimal field for pinning is $20 Gauss$. As we work in very low fields, it is hard to understand how the results can be explained using a model that is built on pinning phenomena.

This brings us to what we belive is the only consistant interpratation of our data. According to the Uemura relation $T_c \propto 1/\lambda_{ab}^2$. In MKS $VF = 4\pi\chi$ and using equation 3.8 we get $VF \propto \frac{a^2}{\lambda^2}$. The linear relation of the VF on T_c is naturally explained if we assume that the variation of the VF originates only in the change in the penetration depth. Although it is not clear how a, the length scale representing the size of the basic superconducting block, is the same for all samples we checked, we understand the linear relation of the VF on T_c as an independent verification of the Uemura plot. In Fig 3.17 we show T_c vs. VF and vs. σ for all the CLBLCO, LSCO and YBCO
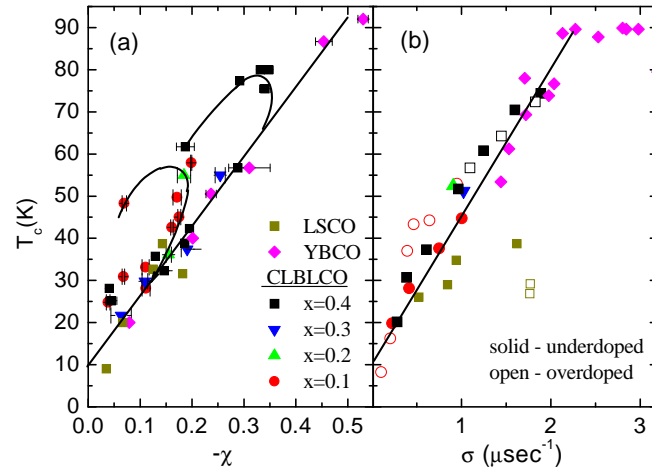
Figure 3.17: (a) T_c vs. the VF. (b) T_c vs. the TF-μSR relaxation rate. The LSCO and YBCO data is taken from [32]

samples.

Chapter 4

Discussion

In this chapter we would like to discuss our result in greater detail, and put them in the right context.

4.1   Numerical simulation

To improve our understanding of the muon polarization at base temperature, we performed simulations of a toy model aimed at reproducing the results described above.

A 2D 100×100 square lattice is filled with two kinds of moments, nuclear and electronic. All the nuclear moments are of the same size, they are frozen and they point in random directions. Of the electronic moments only a small fraction p is assumed to be frozen; they represent magnetic regions with uncompensated antiferromagnetic interactions. Since these regions may vary in size, the moments representing them are random, up to a maximum size. The frozen electronic moments induce spin polarization in the other electronic moments surrounding them. Following the work of others
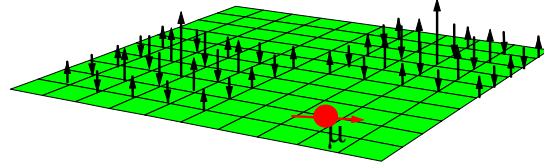
Figure 4.1: Demonstrating the numerical simulations. Two spins (long arrows) are placed on the lattice. They polarize the nearby spins. The muon interacts with the spin by dipolar interaction. Nuclear moments (which participate in the simulation) are not shown.
איור המתאר את תצורת הספינים כפי שנלקחה בסימולציות המחשב שבצענו.

[33], we use decaying staggered spin susceptibility which we take to be exponential, namely,

$$\chi^{'}(\mathbf{r}) = (-1)^{n_x+n_y} \exp(-r/\xi) \tag{4.1}$$

where $\mathbf{r} = n_x a\widehat{x} + n_y a\widehat{y}$ represents the position of the neighbor Cu sites, $\mathbf{a}$ is the lattice vector, and ξ is the characteristic length scale. Because of this decay, at low frozen spin concentration, large parts of the lattice are practically field free (except for nuclear moments). However, the important point is that no clear distinction between magnetic and field free (superconducting) regions exists. This situation is demonstrated in Fig. 4.1.

The muon polarization time evolution in this kind of field distribution is numerically simulated. The interaction between the muon and all the other moments is taken to be dipolar, and ξ is taken to be 3 lattice constants [34, 35]. The dashed line in Fig. 3.1 is a fit to the $T = 350$ mK data, which yields $p = 15\%$ and maximum moment size $\simeq 0.06\mu_B$. As can be seen, the line fits the data very well. However, as expected, the fit is sensitive to $p\xi^2$ only, namely to the effective area of the magnetic islands, so a larger ξ would have resulted in a smaller p. The field distributions and the polarization curve shown in Fig. 3.4 were actually generated using the simulation. In (a) the spin density is 15% while in (b) the density is 35%. In panel (c) of Fig. 3.1 we show the spin polarization for different hole concentrations, varying from 0% to 35% with the same $\xi = 3$. The resemblance between the simulation results as a function of p and the muon polarization as a function of temperature in panel (a) leads us to the conclusion that the freezing process is mostly a growth in the total area of the frozen AF islands.

4.2   Scaling relations

In upper panel of figure 4.2 we show T_c versus the doping in CLBLCO. For different x values there is a different maximal T_c at a different doping level. We define, for every compound, the oxigen doping level as measured from optimal doping:

$$\Delta y = y - y_0$$

where y_0 is the point where T_c is maximal. In that sense, in the CLBLCO system, every x value represents a different compound, meaning that y_0 can be different for different x.
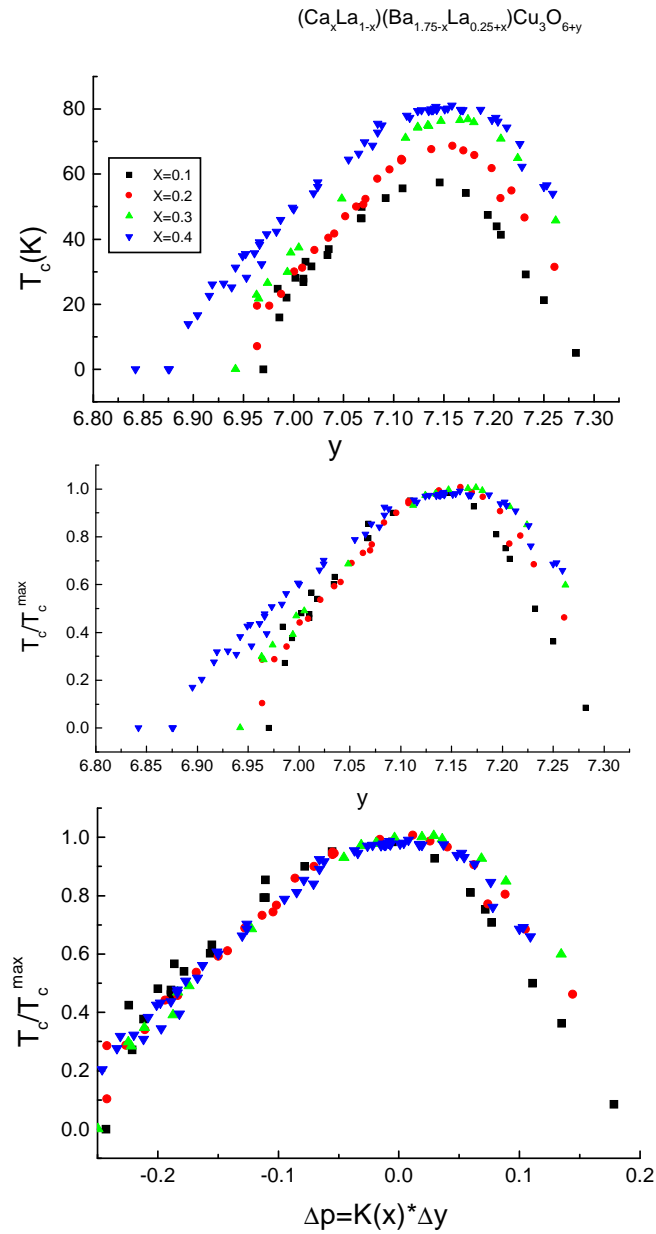
Figure 4.2: The two steps that are made for all the T_c vs. y curves to collapse on one curve.

הצעדים שנדרשים כדי לאחד את עקומות T_c לעומת y לעקומה אחת.

We scale the domes of the upper panel of figure 4.2 by dividing for every x value T_c by T_c^{max} and plot T_c/T_c^{max} vs y. This is presented in the middle panel. In order to make all the curves converge into one, we also need to multiply Δy for every family by a different constant, that we name $K(x)$. Thus, we define $\Delta p = K(x)\Delta y$. T_c/T_c^{max} vs. Δp is shown is the lower panel of figure 4.2. We use the same scaling, built to make the T_c curves to coincide, on the T_g versus y lines. The result for the CLBLCO data is shown in figure 4.3. As one can see all the lines merge into one line!

Encouraged by the success of the scaling relations for the CLBLCO samples, we tried to use the same scaling on other compounds data. The families for which both T_g and T_c data exist beside $(Ca_xLa_{1-x})(Ba_{1.75-x}La_{0.25+x})Cu_3O_y$ [CLBLCO] [36] are $La_{2-y}Sr_yCuO_4$ [LSCO] [4, 5], $Y_{1-y}Ca_yBa_2Cu_3O_6$ [YCBCO] [4], $Bi_{2.1}Sr_{1.9}Ca_{1-x}Y_xCu_2O_{8+y}$ [Bi-2212] [5], and $YBa_2Cu_3O_y$ [YBCO] [37]. T_g in these works was probed using ZF-μSR. Different authors use different fit functions for the determination of T_g. We will show below that this has no bearing on our final conclusion. In this case we define K_f, a different scaling parameter for each compound. We aim to make all the T_c/T_c^{max} domes merge into the curve of simplest cuprate, LSCO. We then use the same scaling on the T_g data, as explained previously. The results are shown in figure 4.4 and the parameters used in the scaling are shown in table 4.1.

We demonstrate that the simultaneous scaling of T_g and T_c is a property of clean superconductors and does not work in all cases. A perfect example for a scaling failure is given by $La_{2-y}Sr_yCu_{1-x}Zn_xO_4$ [LSCZO] [5]. Here Zn is responsible for generating different families by disturbing the uniformity of the CuO_2 planes. As demonstrated in figure 4.5, the scaling transformation that makes all T_c vs. Δp domes merge into one function does not apply for T_g vs. Δp. This suggests that a mechanism with a different energy scale is involved in the reduction of T_c when impurities are present.
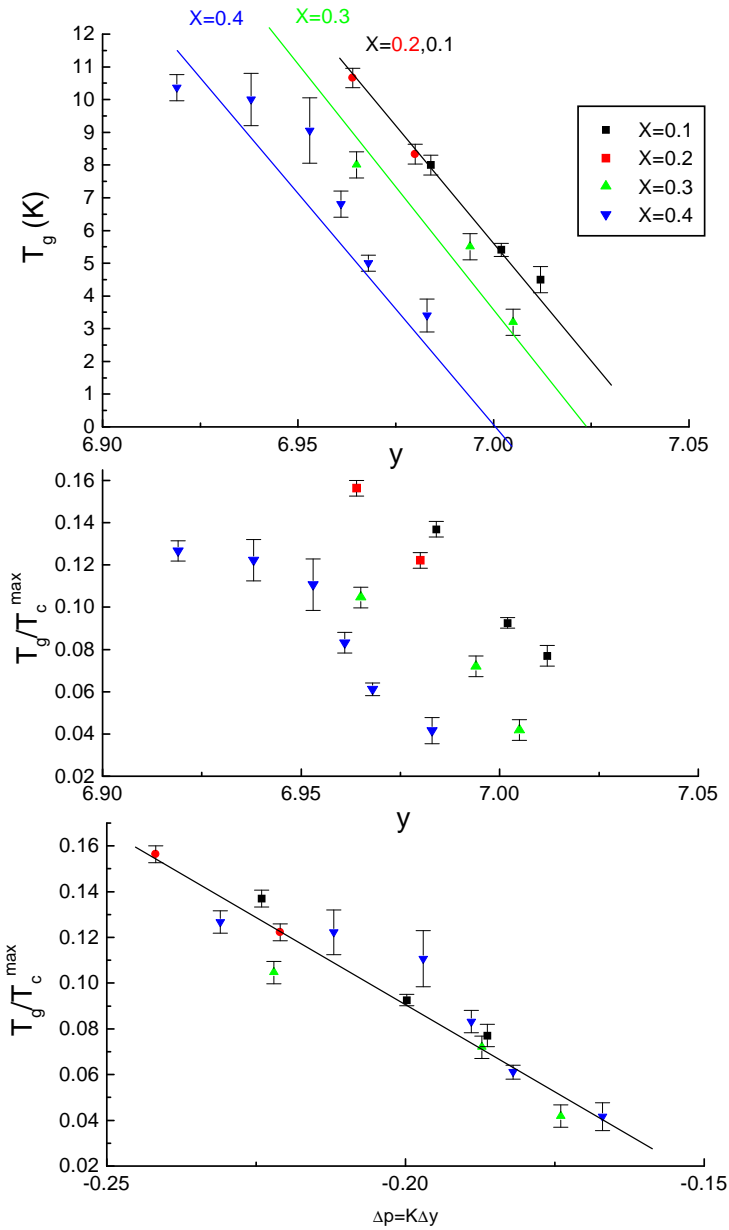
Figure 4.3: The same scaling steps as in the previous figure, now performed on the T_g data.

אותם צעדים כשם שהופיעו בציור הקודם, כעת מבוצעים על נתוני T_g לעומת y.
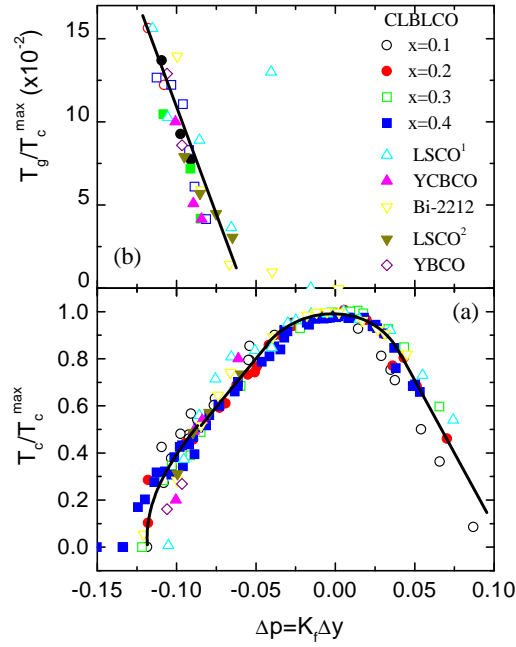
Figure 4.4: (a) T_c/T_c^{max} and (b) T_g/T_c^{max} as a function of $\Delta p = K_f \Delta y$. K_f is chosen so that T_c/T_c^{max} vs. Δp domes of various cuprates families collapse into a single curve. As a consequence T_g/T_c^{max} vs. Δp also collapses into a single line.
יחסי סלום עבור מספר משפחות שונות של על-מוליכים.

From the Uemura relation we know:

$$T_c = Jn_s(\Delta p)$$

In section 1.2 we showed that according to the Boson-Fermion model J, which we identify with J_b, the pair hopping, does not depend on the doping. Thus the variation in T_c originates in variations in the superfluid density. This allows us to write:

$$T_c^{max} = Jn_s(0) \tag{4.2}$$

In this framework the scaling result is:

$$\frac{T_c}{T_c^{max}} = \frac{n_s(\Delta p)}{n_s(0)} \tag{4.3}$$

HTSC Family	P_{opt}	K_f	$T_c^{\max}$
CLBLCO $x = 0.1$	0.18	2.0	58
CLBLCO $x = 0.2$	0.18	1.9	69
CLBLCO $x = 0.3$	0.18	1.8	77
CLBLCO $x = 0.4$	0.18	1.5	80
LSCO	0.16	1.0	38
YCBCO	0.16	1.1	65
Bi-2212	0.16	1.1	44
YBCO	0.16	1.0	93
LSCZO $x = 0.01$	0.16	1.5	26
LSCZO $x = 0.01$	0.18	2	17

Table 4.1: Table showing the optimal chemical doping, the scaling factor, and the maximum T_c for the various compounds presented in Fig. 4.4 The $T_c^{\max}$ (and p_{opt}) of YCBCO is not known, and the values given in the table are assumed. Only two samples of YBCO, for which both T_g and T_c have been measured, are shown.
טבלת הפרמטרים שבהם השתמשנו בסלום של הנתונים הניסיוניים עבור משפחות שונות של על-מוליכים.

Although we do not know the form of $n_s(\Delta p)$, equation 4.3 represents a universal relation for the cuprates. If we use the result of section 1.2.2, then

$$T_g = J_t f(\Delta p)$$

where f is an unknown function of the doping. After the scaling we get:

$$\frac{T_g}{T_c^{max}} = \frac{J_t}{J_b} \frac{f(\Delta p)}{n_s(0)}$$

There are two conditions for the curves to coincide: First, we divided two energy scales, J_t and J_b, so for the scaling to work J_b must be proportional to J_t. Furthermore, we obtain a relation between J_b and J_t that is common to all compounds. Second, the horizontal axis represents a line on which n_s/n_s^{max} for all the different compounds is equal, the fact that the T_g lines coincide on the same axis indicates that T_g is a function of the superfluid density and does not depend directly on the doping:

$$T_g = J_t f\left(\frac{n_s(\Delta p)}{n_s(0)}\right)$$

This can have far reaching implications in understanding the cluster spin glass physics.

The success of the simultaneous scaling of T_c and T_g for all the pure compounds discussed above, suggests that the same energy scale J controls both the supercon- ducting and magnetic transitions in all cuprates. We can compare this result to the prediction of the Boson-Fermion model. Different compounds can have different t and U parameters, where t is the hopping integral and U is the on-site interaction of the Hubbard model, but according to figure 1.2, the ratio J_b/J_t, varies by no more than 50% over all the range in which the holes bind into pairs. Our data suggests an even stronger constraint, that J_b/J_t is common to all the compounds.
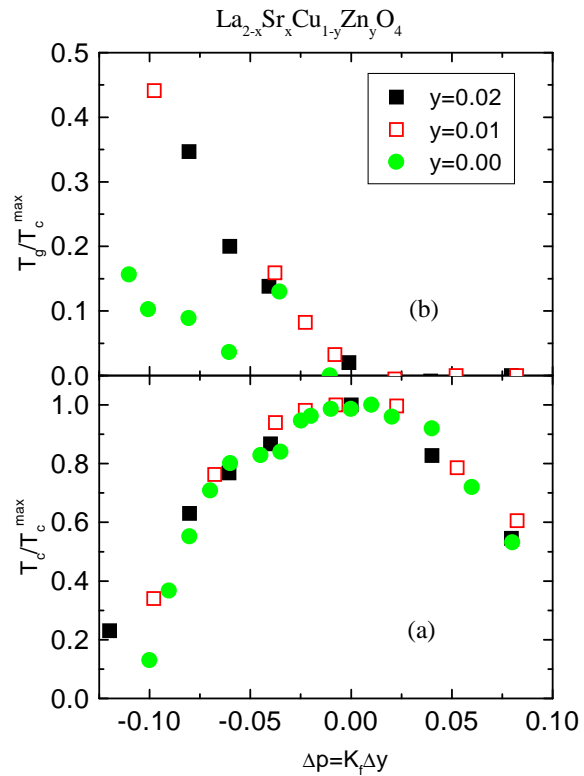
Figure 4.5: (a) T_c/T_c^{max} and (b) T_g/T_c^{max} as a function of $\Delta p = K_f \Delta y$. K_f is chosen so that T_c/T_c^{max} vs. Δp domes for various $La_{2-y}Sr_yCu_{1-x}Zn_xO_4$ compounds, representing impure cases, merge into a single curve. The same scaling does not apply to T_g.

הדגמה של כשלון יחסי הסלום במקרה של חומר בו מישורי ה-CuO_2 מסוממים ב-Zn.

Chapter 5

Conclusions

Using TF-μSR we measured the penetration depth at base temperature of CLBLCO samples. We found that these samples satisfy perfectly the Uemura relation, meaning that $T_c \propto n_s$, where n_s is the superfluid density. We also verified the Uemura relation using magnetization measurements at low fields. Using the special properties of the CLBLCO system we were able to show that what governs T_c is the superfluid density and not the chemical doping level.

We performed ZF-μSR measurements on CLBLCO underdoped samples. We learn that these samples have a unique magnetic ground state which is a cluster spin-glass. Magnetism and superconductivty co-exist on a microscopic length scale. We also constructed the magnetic phase diagram of the CLBLCO system.

Using a scaling relation we were able to show that a single energy scale, J, governs both the superconcting and the magnetic phases, so T_c can be written as $T_c = J \times n_s$ were J can vary between different cuprates.

References

[1] F. Mila and T. M. Rice, Phys. Rev. **B40**, 11382 (1989).

[2] Takigawa *et. al.*, Phys. Rev. Lett. **63**, 1865 (1989), Takigawa *et. al.*, Phys. Rev. **43**, 247 (1991).

[3] P. Mendels *et. al.*, Europhysics Lett., 46, 678 (1999).

[4] C. Niedermayer *et al.* Phys. Rev. Lett. **80**, 3843 (1998).

[5] C. Panagopoulos *et. al.*, Phys. Rev. **B66**, 064501 (2002).

[6] Altman E. and Auerbach A., Phys. Rev. **B65**, 104508 (2002).

[7] Auerbach A. and Altman E., Int. J. Modern Phys. **B15**, 2509 (2001).

[8] P. M. Chaikin and T. C. Lubensky, Principles of condensed matter physics, Cambridge press, New York (1995).

[9] V. J. Emery and S. A. Kivelson, Nature **374**, 434 (1995).

[10] B. Keimer *et. al.*, Phys. Rev. Lett. **45**, 7430 (1992).

[11] O. P. Vajk *et. al.*, Science **295**, 1691 (2002).

[12] F. C. Zhang and T. M. Rice, Phys. Rev. **B37**, 3759 (1988).

[13] J. H. Cho *et. al.*, Phys. Rev. **B46**, 3179 (1992).

[14] F. C. Chou *et. al.*, Phys. Rev. Lett. ,2323 (1993).

[15] Julien M. H. el. al., Phys. Rev. Lett. **83**, 604 (1999).

[16] Matsuda M., Phys. Rev. **B46**, 3179 (2000).

[17] D. Goldschmidt *et al.*, Phys. Rev. B **48**, 532 (1993).

[18] S. J. Blundell, cond-mat/0207699, (2002).

[19] W. Barford and J. M. F. Gunn, Physica **C156**, 515 (1988).

[20] Yeshurun Y. *et. al.*, Rev. Mod. Phys. **68**, 911 (1996).

[21] *Muon Science*: Muons in Physics, Chemistry and Materials, Eds S. L. Lee, S. H. Kilcoyne and R. Cywinski (Institute of Physics, London), 1999.

[22] As long as $\gamma_\mu H < \nu$, where ν is the fluctuation rate.

[23] M. I. Larkin *et al.*, Phys. Rev. Lett. **85**, 1982 (2000).

[24] C. Bernhard *et al.*, Phys. Rev. **B58**, 8937 (1998).

[25] P. Mendels (private communication).

[26] A moment of $1\mu_B$ will induce a 1G field at a distance of $\sim 20\mathring{A}$. This field is equivalent to the nuclear moments background.

[27] C. P. Poole, Handbook of Superconductivity, Academic Press, (2000).

[28] B. M. Smolyak *et. al.*, Supercond. Sci. Technol. **7**, 427 (1994).

[29] D. Wohlleben, G. Michels and S. Ruppel, Physica C **174**,242 (1991).

[30] K.A. Muller, M. Takashige and J. G. Bednorz, Phys. Rev. Lett. **58** , 1143 (1987).; C. Ebner and D. Stroud, Phys. Rev. B **31**, 165 (1987).

[31] Y. Yeshurun and A. P. Malozemoff, Phys. Rev Lett. **60**, 2202 (1988).

[32] Y. J. Uemura, Physica **C**, 194 (1997).

[33] A. J. Millis, H. Monien, and D. Pines, Phys. Rev. B **42**, 167 (1990); J. Bobroff et al., Phys. Rev. Lett. **79**, 2117 (1997); M. H. Julien *et al*, Phys. Rev. Lett. **84**, 3422 (2000).

[34] C. Howald *et al.*, cond-mat/0101251, J.M. Tranquada *et al*, Nature **375**, 561 (1995); V.J. Emery and S.A. Kivelson, Physica C **209**, 597 (1993).

[35] B. Nachumi *et al.* Phys. Rev. Lett. **77**, 5421 (1996); S. H. Pan *et al.*, Nature **401**, 746 (2000).

[36] A. Kanigel *et. al.*, Phys. Rev. Lett **88**, 137003 (2002).

[37] S. Sanna *et. al.*, Solid. State. Comm. **126**, 85 (2003).

[38] P. Mendels *et al.*, Phys. Rev. B **49**, 10035 (1994).

[39] J. Bobroff *et al.*, Phys. Rev. Lett. **86**, 4116 (2001).

[40] The density of hole per plane is $p = -0.205 + y/3$.

[41] O. Chmaissem *et al.*, Phys. Rev. B **63**, 174510 (2001).

[42] A. Knizhnik *et al.*, Physica C **321**, 199 (1999).

[43] A. Knizhnik *et. al.*, Physica **C321**, 199 (1999).

[44] S. C. Zhang *et al.*, Phys. rev. **B60**, 13060 (1999); E. Altman and A. Auer-bach, cond-mat/0108087.

[45] Y. J. Uemura *et. al.*, Phys. Rev. Lett. **62**, 2317 (1989)